Inertial displacement of a domain wall excited by ultra-short circularly polarized laser pulses

T. Janda,[1] P. E. Roy,[2] R. M. Otxoa,[2]
Z. Šobáň,[3] A. Ramsay,[2] A. C. Irvine,[4] F. Trojanek,[1] M. Surýnek,[1] R. P. Campion,[5]
B. L. Gallagher,[5] P. Němec,[1] T. Jungwirth[3,5] J. Wunderlich,[3,2,#]

[1]Faculty of Mathematics and Physics, Charles University,
Ke Karlovu 3, 121 16 Prague 2, Czech Republic
[2]Hitachi Cambridge Laboratory, J. J. Thomson Avenue,
Cambridge CB3 0HE, United Kingdom
[3]Institute of Physics, Academy of Sciences of the Czech Republic,
Cukrovarnická 10, 162 00 Praha 6, Czech Republic
[4]Microelectronics Research center, Cavendish Laboratory, University of Cambridge,
Cambridge CB3 0HE, United Kingdom
[5]School of Physics and Astronomy, University of Nottingham,
Nottingham NG7 2RD, United Kingdom

[#]To whom correspondence should be addressed; E-mail: jw526@cam.ac.uk.

March 28, 2017

Domain wall motion driven by ultra-short laser pulses is a prerequisite for envisaged low-power spintronics combining storage of information in magneto-electronic devices with high speed and long distance transmission of information encoded in circularly polarized light. Here we demonstrate the conversion of the circular polarization of incident femtosecond laser pulses into inertial displacement of a domain wall in a ferromagnetic semiconductor. In

our study we combine electrical measurements and magneto-optical imaging of the domain wall displacement with micromagnetic simulations. The optical spin transfer torque acts over a picosecond recombination time of the spin-polarized photo-carriers which only leads to a deformation of the internal domain wall structure. We show that subsequent depinning and micro-meter distance displacement without an applied magnetic field or any other external stimuli can only occur due to the inertia of the domain wall.

DWs driven by short field (*1*) or current (*2, 3*) pulses of length $\sim 1 - 10$ ns and moving at characteristic velocities reaching $\sim 0.1 - 1$ μm/ns (*4*) are displaced over the duration of the pulse by distances at least comparable but typically safely exceeding the domain wall width. In this regime inertia, causing a delayed response to the driving field and a transient displacement after the pulse, is not the necessary prerequisite for the device operation and is rather viewed as negative factor. It can set the operation frequency limit of the DW device and potentially affect precise positioning of the DW by the driving pulse. Realizing massless DW dynamics is therefore one of the goals in the research of field-driven and current-driven DWs (*5*).

The aim of our study is the demonstration of a micrometer-scale DW displacement by circularly-polarized, ultra-short laser pulses (LPs). Our experiments are in the regime where the external force generated by the LP acts on the picosecond time-scale over which the expected sub-nanometer DW displacement would be orders of magnitude smaller than the DW width and insufficient for any practical DW device implementation. Inertia allowing for a free transient DW motion is the key here that enables the operation of the DW devices in the regime of the ultra-short optical excitations, rather than being a factor limiting the operation of the opto-spintronic DW devices.

Our study links the physics of inertial DW motion with the field of optical recording of magnetic media. The manipulation of magnetism by circularly polarized light, demonstrated

already in ferrimagnets (*6*), transition metal ferromagnets (*7*), and ferromagnetic semiconductors (*8*), has become an extensively explored alternative to magnetic field or current induced magnetization switching. Our work demonstrates that optical recording can in principle be feasible at low power when realized via an energy-efficient DW displacement driven by ultra-short LPs and without the need to heat the system close to the Curie temperature.

The III-V based ferromagnetic semiconductor used in our study is an ideal model system for the proof of concept demonstration, as well as, for the detailed theoretical analysis of the DW dynamics in this new regime. DWs in out-of-plane magnetized (Ga,Mn)(As,P) have a simple Bloch wall structure with low extrinsic pinning (*9*). The non-thermal optical spin transfer torque (oSTT) mechanism which couples the circular polarization of the incident light to the magnetization via spin-polarized photo-carriers is microscopically well understood in this ferromagnetic semiconductor material (*10*). In our experiments, individual circularly polarised ~ 100 fs short LPs at normal incidence and separated by ~ 10 ns expose an area with a single DW. As illustrated in figure 1A, the generated perpendicular-to-plane spin-polarised photoelectrons exert the oSTT only in the region with an in-plane component of the magnetization, i.e. in the DW. The action of the oSTT is limited by the photoelectron recombination time ~ 10 ps.

To probe the inertial DW motion, we make use of elastic properties of a uniformly propagating DW. In this case, the DW propagates continuously and remains connected so that local DW pinning affects the entire wall over its whole extension. First, the Oersted field generated in a stripe line above the magnetic bar nucleates a reversed magnetic domain. Then, a single DW is driven towards a cross structure by a small external magnetic field of a slightly larger magnitude than the propagation field B_{PR}. The low B_{PR} of ~ 0.1 mT found in our bar devices patterned from an epitaxially grown $Ga_{0.94}Mn_{0.06}As_{0.91}P_{0.09}$ 25 nm thick film implies a very small DW pinning on structural defects and inhomogeneities. In this case, DW propagation is

uniform and a straight DW becomes pinned at the entrance of the cross structure as shown in figure 1B. To continue the DW propagation through the cross, the DW must increase its length which is accompanied by an increase in its magnetic energy. This results in a restoring force which can be expressed in terms of a virtual restoring field $B_{\mathrm{R}}(x)$ that depends on the position x of the DW. Here, $B_{\mathrm{R}}(x)$ acts as to always drive the DW back to the cross entrance. The magnetic field driven expansion of a DW pinned at the cross entrance is analogous to the inflation of a two-dimensional soap-bubble (see figure 2A). The DW depins when the applied field exceeds the maximum restoring field $B_{\mathrm{R}}^{\mathrm{max}}$ (*11*). Within this model, $B_{\mathrm{R}}(x)$ reaches its maximum value $|B_{\mathrm{R}}^{\mathrm{max}}| = \sigma/(M_{\mathrm{S}} \cdot w)$ at the cross center at $x = 0$ (figure 3A) and the DW can only depin once it passes the cross center. Here, $\sigma = 4\sqrt{AK_{\mathrm{E}}}$ is the DW energy per unit area, K_{E} the effective perpendicular anisotropy coefficient, A the exchange stiffness, M_{S} the saturation magnetization and w is the width of the bar. The DW can be depinned from the cross by either an applied magnetic field $B_{\mathrm{A}} > |B_{\mathrm{R}}^{\mathrm{max}}|$ or by the oSTT. We can therefore use $|B_{\mathrm{A}}| \leq |B_{\mathrm{R}}^{\mathrm{max}}|$ to calibrate the strength of the oSTT.First, however, we have to confirm the elastic nature of DWs in our devices, and verify the applicability of the bubble-like DW model of figure 2A.

Results

Elastic domain wall pinning. We performed magnetic field driven DW motion experiments without optical excitation. Depinning fields for three different devices with bar widths of 2, 4 and 6 μm are shown in figure 3C as a function of the inverse bar width. The slope of the linear fit agrees with that obtained from the measured effective perpendicular anisotropy, $K_{\mathrm{E}} = 1200$ J/m^3, the saturation magnetization, $M_{\mathrm{S}} = 18$ kA/m, and assuming the exchange stiffness, $A = 50$ fJ/m, which is a reasonable estimate for our GaMnAsP film (*9*). The elastic behaviour of the $\pi\sqrt{A/K_{\mathrm{E}}} \sim 20$ nm wide DW is also confirmed by MOKE images of the 6 μm wide bar device shown in figure 2B-D . In figure 2B, the DW bends into a bubble-like shape under the

influence of an applied field B_{A} = 0.25 mT. Figure 2C shows that the restoring field drives the DW back to the cross-entrance after B_{A} is turned-off. Figure 2D displays the difference between the two MOKE images in figure 2B and figure 2C, confirming the bubble like shape of the DW. In addition, anomalous Hall effect (AHE) measurements performed on the 4 μm device under an alternating field excitation$B_{\mathrm{A}} = B_0|\sin(\omega \cdot t)|$ also confirm the elastic DW behaviour (figure 3B). If B_0 does not exceed $|B_{\mathrm{R}}^{\mathrm{max}}|$, e.g., for $B_0 = 0.2$ mT (green), and $B_0 = 0.3$ mT (blue), the periodic variation of the AHE signal indicates that the DW is at the position x where $B_{\mathrm{R}}(x)$ and $B_{\mathrm{A}}(t)$ compensate. The residual AHE signal at $B_{\mathrm{A}} = 0$ of about 10 $\%$ of the maximum AHE signal at reversed saturation (DW depinned from the cross) corresponds to the AHE-response for the magnetization distribution with a straight DW located at the cross entrance. (For more details see Supplementary Note 1.)

Helicity dependent domain wall excitation by ∼100 fs laser pulses. We now combine the elastic pinning properties of the DW at the cross with the light induced excitation experiments in order to proof the inertial character of the oSTT-induced DW motion. The basic idea of our experiment is to exploit the elastic restoring force which acts continuously throughout the entire cross (of a width up to 6 μm in our study) against the expansion of the DW which is driven by individual $\sim$ 100 fs LPs. The photo-generated electrons can transfer their spin to the magnetization only during their $\sim$ 10 ps lifetime which is 3 orders of magnitude shorter than the pulse separation time of $\sim$ 10 ns. The measurements shown in figure 3 are performed at a 90 K sample temperature. We obtain similar results when performing the measurements also at higher (95 K) and at lower (75 K) sample temperatures, as shown in Supplementary Note 1. At these temperatures, LPs with a wavelength λ = 750 nm excite photo-electrons slightly above the bottom of the GaAs conduction band so that for a circularly polarized incident light, photo-electrons become spin-polarized with the degree of polarization approaching the maximum theoretical value of 50% (*12*). To avoid the difficulty with aligning our $\sim$ 1 μm

Gaussian spot on top of a ~ 20 nm wide DW, we employ the experimental procedure sketched in figure 4A. First, a straight DW is positioned at the cross entrance. Then, the LP spot is placed 10 μm away from the DW on the reversed domain side and a magnetic field B_{A} with $B^0_{\mathrm{DP}}(\approx +0.4\ mT) > B_{\mathrm{A}} > B_{\mathrm{PR}}(\approx -0.1mT)$ is applied. (B^0_{DP} is the DW depinning field without LP irradiation.) In this field range and without LP irradiation, the DW remains pinned at the cross entrance. The LP spot is then swept at a rate of ~ 2 μm/ms for 20 μm along the bar so that the initial DW position is crossed by the spot and approximately $\sim 10'000$ ultra-short LPs time-separated by $\sim$10 ns expose the DW. The lowest applied magnetic field at which the DW depins from the cross in the presence of LPs is labeled B_{DP}. The dependencies of B_{DP} on the LP energy density for circularly polarized σ^+, σ^- and linearly polarized σ^0 LPs are shown in figure 4B. First, we recognize a reduction of B_{DP} with increasing energy density for all three LP polarizations. In case of the linear polarization, i.e., without the oSTT contribution, we attribute the reduction of $B_{\mathrm{DP}}(\sigma^0)$ only to the LP induced sample heating. Importantly, we do not observe DW depinning without applying $B_{\mathrm{A}} > 0$ up to the highest LP energy densities used in our experiments of more than $\sim$ 30 mJ/cm^2. At large LP energy densities above $\sim$ 20 mJ/cm^2 we observe a saturation of $B_{\mathrm{DP}}(\sigma^0)$ with increasing LP energy density implying that LP heating does not increase anymore. We assign this behaviour to the saturation of photo-carriers generated at very high LP energy densities.

For circularly polarized LPs, an additional contribution from the oSTT is present. We observe for all measured LP energy densities that $B_{\mathrm{DP}}(\sigma^+) < B_{\mathrm{DP}}(\sigma^0) < B_{\mathrm{DP}}(\sigma^-)$ for the positive magnetization orientation of the nucleated domain. In case of σ^+ polarised LPs and at high enough LP energy densities (above 12 mJ/cm^2) the DW depins without an applied magnetic field (and even at small negative applied magnetic field which opposes DW expansion).

For σ^- polarized LPs and the same initial domain configuration, we do not observe the zero-field DW depinning up to the highest LP energy density used in our experiments. Instead,

we again observe saturation of $B_{\mathrm{DP}}(\sigma^-)$ above $\sim$ 20 mJ/cm^2. We attribute the difference in the saturation values of $B_{\mathrm{DP}}(\sigma^-)$ and $B_{\mathrm{DP}}(\sigma^0)$ to the effect of the oSTT acting against depinning for σ^- polarized LPs.

We estimate the LP heating related temperature increase by comparing $B_{\mathrm{DP}}(\sigma^0$, LP energy density, $T = 90$ K) measured at constant 90 K base temperature with the temperature dependence of $B^0_{\mathrm{DP}}(T)$ without LP irradiation. We found that for LP energy densities of up to 35 mJ/cm^2, the temperature increase does not exceed the Curie temperature of ~ 115 K of the GaMnAsP film.

The differential MOKE image in figure 4C shows an example of the domain configuration after the DW has depinned from the cross entrance by optical excitation in conjunction with a constant applied magnetic field B_{A} which is larger than the DW propagation field of the bar outside the cross. After depinning from the cross irradiated by polarized LPs, the DW becomes pinned again at a second cross which was not irradiated during the experiment. Figure 4D shows the final domain configuration after DW depinning by σ^+ polarised LPs at zero applied magnetic field. In this case, the σ^+ polarized LPs depin and drive the DW forward to the final irradiated spot position.

Inertial domain wall propagation. From the measurements shown in figure 4 we can conclude that for the given initial domain configuration, the oSTT generated by σ^+ (σ^-) polarised LPs assists (opposes) DW depinning. The measurements confirm that only σ^+ polarised LPs can move the DW beyond the maximum of the pinning barrier at the cross center. Considering the $\sim$ 100 fs short and $\sim$10 ns time-seperated LPs, depinning of the DW by the oSTT becomes only possible if the elastically pinned DW propagates forward in between successive LPs. Depinning by a DW motion without inertia would require DW velocities of more than 1 km/s which are unrealistically high for the DW motion in GaMnAsP films where the maximum magnon velocity is of similar magnitude and where we have observed and calculated

Walker break down velocities ~ 10 m/s for the oSTT, current and field driven DW motion (*9*). (See also Supplementary Note 2.)

To verify our interpretation, we repeated our measurements at the inverted magnetization configuration in which the reversed magnetization of the nucleated domain points in the negative ($-m_z^{\mathrm{R}}$) direction. In this case, the oSTT should act in the opposite direction. Indeed, we observe the opposite helicity dependency in our experiments. Figure 5 shows measurements on a 4 μm wide device comparing the two magnetisation configurations. The consistency found between $B_{\mathrm{DP}}(\sigma^{+(-)}, +m_z^{\mathrm{R}}) \approx -B_{\mathrm{DP}}(\sigma^{-(+)}, -m_z^{\mathrm{R}})$ and $B_{\mathrm{DP}}(\sigma^{0}, +m_z^{\mathrm{R}}) \approx -B_{\mathrm{DP}}(\sigma^{0}, -m_z^{\mathrm{R}})$ confirms the oSTT mechanism and the high reproducibility of our measurements.

Note, that a heat-gradient can in principle also drive the DW motion (*13*). The heat-gradient driven motion can become helicity dependent if the light absorption in the two adjacent magnetic domains is helicity-dependent due to the magnetic circular dichroism (MCD). In our experiments, such a scenario is unlikely because about $\sim 98\%$ of the LP light penetrates through the 25nm thick magnetic GaMnAsP film and is absorbed and transformed into the heat in the GaAs substrate with no dependence on the helicity.

An indication that the MCD is not the origin of the observed helicity dependent DW depinning is given by helicity-dependent DW experiments shown in the Supplementary Note 3. The experiments are performed at photon-energies ranging from below the band-gap up to high energies where the net spin-polarization of photo-electrons is reduced due to the excitation from the spin-orbit split-off band. We do not observe the helicity-dependent DW depinning at photon-energies where MCD of GaMnAsP is still present while simultaneously the photoelectron polarisation is strongly reduced.

To investigate the effect of the MCD on the helicity dependent DW motion in more detail, we present additional experiments in the Supplementary Note 3 which allow us to identify the sign and estimate the magnitude of the temperature gradient generated by the MCD between

two opposite magnetized domains. We found that the MCD-generated heat-gradient is smaller than the helicity independent heat-gradient generated by the Gaussian LP spot, and more importantly, that the DW motion induced by the MCD is in the opposite direction to the observed helicity dependent DW motion. This excludes unambiguously the MCD as the origin of our experimental observations.

To further analyze heat-gradient related DW drag effects due to the non-uniform heating by the Gaussian-shaped LP spot, we have performed measurements with opposite laser spot sweep directions. In this case, the heat-gradient with respect to the initial DW position is inverted. As shown in the Supplementary Note 3, sweeping the LP spot along the bar from an initial position outside of the nucleated domain to the final position in the nucleated domain does not change the helicity dependency of the depinning field. Additional measurements on devices with 2 and 6 μm wide bars have, apart from the stronger (weaker) DW pinning strength and larger (smaller) temperature increase from LP heating in the 2 μm (6 μm) device, also confirmed that $B_{\mathrm{DP}}(\sigma^{+(-)}) < B_{\mathrm{DP}}(\sigma^{0}) < B_{\mathrm{DP}}(\sigma^{-(+)})$ for $+(-)m_z^{\mathrm{R}}$.

We now support our interpretation of the experiments by 1-dimensional Landau-Lifshitz-Bloch (LLB) numerical simulations of the magnetization $\mathbf{m}$ (*14*), coupled to the precessional dynamics of the spin-polarized photo-carrier density, $\mathbf{s}$ (*10*):

$$\frac{\partial \mathbf{m}}{\partial t} = -\gamma \mathbf{m} \times \mathbf{H}_{\mathrm{eff}} - \frac{\gamma \alpha_{\perp}}{m^2} \mathbf{m} \times (\mathbf{m} \times \mathbf{H}_{\mathrm{eff}}) + \frac{\gamma \alpha_{||}}{m^2} (\mathbf{m} \cdot \mathbf{H}_{\mathrm{eff}}) \mathbf{m} \tag{1}$$

$$\frac{\partial \mathbf{s}}{\partial t} = \frac{-J_{\mathrm{ex}}}{\hbar m_{\mathrm{eq}}} \mathbf{s} \times \mathbf{m} + R(t)\hat{n} - \frac{\mathbf{s}}{\tau_{\mathrm{rec}}} \tag{2}$$

In Eq. (1), **m**=**M**(T)/M_0, with M_0 denoting the saturation magnetization at zero temperature and γ is the gyromagnetic ratio. The first, second and third terms describe the precession, transverse relaxation and longitudinal relaxtion of **m**, respectively. The effective field

$\mathbf{H}_{\text{eff}} = \mathbf{H}_{\text{d}} + \mathbf{H}_{\text{ex}} + \mathbf{H}_{\text{mf}} + \mathbf{H}_{\text{k}} + \mathbf{H}_{\text{OSTT}} + \mathbf{H}_{\text{r}}$ comprises demagnetizing field, exchange field, internal material field related to longitudinal magnetization relaxation, uniaxial magnetocrystalline anisotropy field, oSTT field and a geometrical pinning field, respectively. The two parameters $\alpha_{\perp}(T)$ and $\alpha_{||}(T)$ represent the transverse and longitudinal damping, respectively. The oSTT from **s** on **m** is taken into account by $\mathbf{H}_{\text{OSTT}} = \frac{J_{\text{eff}}(T)}{\mu_0 m_{\text{eq}} M_0}\mathbf{s}$ (with $J_{\text{eff}}(T) = J_{\text{ex}} m_{\text{eq}}^2$). For more details see Supplementary Information.

Eq. (2) describes the time-evolution of the spin polarized photo-electron density **s**. The first term is the precession of **s** around the exchange-field of $\mathbf{m}$ with the coupling strength J_{ex}; m_{eq} is the equilibrium magnetization normalized by the zero temperature saturation magnetization M_0. The second term describes the spin-polarised photo-electron injection rate $R(t)$, which is non-zero only during the $\sim$ 100 fs LP, and $\hat{n}$ is the helicity dependent spin-polarization of the injected electrons. Depending on the light-helicity, $\hat{n}$ is $[0\ 0 \pm 1]$. The last term describes the decay of the spin density, determined primarily by the recombination time of the photo-electrons, τ_{rec}.

In the simulations, we consider a Bloch DW subjected to LPs and the restoring field $B_{\text{R}}(x)$ as in figure 3A. $B_{\text{R}}^{\text{max}}$ was set to a reduced value of 0.1 mT due to heat (deduced from figure 4B and described in the Supplementary Information). Figures 6 A,B show the simulated time evolution of **m** and **s** at the initial DW center during and after the application of a single 150 fs pulse with σ^+ ($\hat{n}$=[0 0 1]) polarization.

In figure 6A, the fast precession of **s** around the exchange field of **m** takes place until the photo-electrons recombine. Only during this short time, angular momentum is transfered to **m**. The precession of **s** is much faster than the dynamics of **m** so that a significant change of $\mathbf{m}$ due to the precession around $\mathbf{H}_{\text{eff}}$ happens *after* the photo-electrons recombined. Figure 6B shows the time evolution of $\mathbf{m}$ at the center of the initial DW ($\mathbf{m}$ is initially directed along $+\hat{\mathbf{y}}$ for the Bloch DW). During the short oSTT, **m** is only weakly disturbed from its equilibrium direction.

It takes ~ 1 ns before it is rotated towards the $\hat{\mathbf{z}}$ axis. At this time, the center of the initial DW becomes part of the reversed domain and the DW has shifted by half width. The deformation of the moving DW from the equilibrium Bloch DW profile is shown in figure 6C. The deformation $\Delta\mathbf{m}$ is obtained by subtracting the moving DW from the undisturbed Bloch DW profile after having shifted the center positions of the two DWs to $x = 0$. Shortly after the LP exposure at $t = 50$ ps, the DW magnetisation is strongly distorted. The simulation indicates that even after 5 ns, $\Delta m_x(0) \approx 0.15$, so that the original Bloch DW is still deformed towards a Néel DW. The deformation of the DW from its equilibrium profile long time after the LP was applied causes magnetization precession around the arising effective fields and keeps the DW moving. The photo-electrons only distort the DW while its subsequent motion is driven by the relaxation of the DW towards its equilibrium profile. In figure 6D, the DW position versus time is plotted during the first three LPs. As can be seen, the entire DW moves predominantly between and not during the pulses.

A calculation confirming the depinning of the DW from the cross is shown in Supplementary Note 2. Here, oSTT pulses are applied until the DW reaches the cross center and overcomes the maximum value of the geometric pinning potential. Our simulations fully confirm the experimental observations and the inferred picture in which the inertial motion is responsible for the DW displacement driven by the ultra-short LPs.

Discussion

In summary, we have shown photon-helicity dependent inertial DW motion excited by ultra-short circularly polarized laser pulses. We found that the domain wall only deforms during the short excitation. After excitation, the DW propagates self-propelled driven by its relaxation back to the unperturbed DW profile. We note that the helicity dependent DW motion can be also realized by a continuous light excitation as shown in Supplementary Note 3. However, LP-

excited inertial DW motion is less affected by pinning and, therefore, more efficient than DW motion excited by continuous and lower energy-density light. This is due to the fast initial acceleration of the heavily deformed DW shortly after the pulse. We also remark that the LP induced helicity dependent DW motion is not limited to diluted magnetic semiconductors. The oSTT induced DW motion may also be realized in heterostructures, where the spin-polarised photo-carrier excitation and spin transfer torque are spatially separated, e.g., when spin-polarized photo-electrons are injected from an optically active semiconductor into an adjacent thin ferromagnetic film. In this case, the oSTT can be equally efficient as found in our present study since the total magnetic moment of a $\sim$ 1nm thin magnetic transition metal film is comparable to the total magnetic moment of our 25 nm thick diluted magnetic semiconductor film with $\sim$ 5% Mn doping. Indeed, the DW motion in a ferromagnetic film driven by spin-polarized currents applied electrically in the direction perpendicular to the film-plane has been recently proposed (*15*) and experimentally observed, showing a very fast DW motion (*16*) and low driving current densities (*17*). Our concept represents an optical analogue to these electrical driven DW experiments with the potential of delivering orders of magnitude shorter while still highly efficient spin torque pulses.

Data availability

The datasets generated during and/or analysed during the current study are available from the corresponding author on reasonable request.

Acknowledgements

We acknowledge support from European Metrology Research Programme within the Joint Research Project EXL04 (SpinCal); from EU ERC Synergy Grant No. 610115, from the Ministry of Education of the Czech Republic Grant No. LM2015087, from the Grant Agency of the

Czech Republic under Grant No. 14-37427G, and by the Grant Agency of Charles University in Prague Grants no. 1360313 and SVV2015260216.

Methods

Experimental setup. We use a wide-field magneto-optical microscope to monitor our magnetic bar devices, and to identify DW nucleation and DW position. The magneto-optical polar Kerr effect measured with linearly polarized light of $\lambda = 525$ nm is used to visualize the magnetization distribution in our bar devices. The $\sim$ 100 fs short LPs with 12.5 ns separation time between successive pulses are generated by a Ti:Saphire laser and focused to a $\sim$ 1 μm wide spot by an objective lens which is mounted to a 3D piezo-positioner to enable the precise alignment of the laser spot to the magnetic bar device.

Computational geometry and simulation procedure. Our simulation is based on the Landau-Lifshitz-Bloch (LLB) approach (*14*). We consider a one-dimensional bar with 4095 x 1 x 1 computational cells composing a structure. The cell dimension is 4 nm x 4 μm x 25 nm. A Bloch DW is initialized in the center of the bar and is let to relax quickly with strong damping by setting a large damping parameter λ=0.9. (See Supplementary Note 2.) This configuration is then used as a starting configuration for the simulations of domain wall motion under the light pulses. Once the domain wall is prepared, circularly polarized light is pulsed at a rate of 80 MHz. The length of each pulse is set to 150 fs. For the simulation of the depinning process, the spin-polarized carrier injection rate is $R = 1.225 \times 10^{39}\mathrm{m}^{-3}\mathrm{s}^{-1}$. This order of magnitude for R is required for the DW to escape the elastic pinning potential. The equivalent pulse power corresponds to the LP energy density of 5.6 mJ/cm^2 assuming a skin depth of 1 μm. At this energy density, helicity dependent DW motion becomes evident in the experiments, cf., Figs. 4c, 5. Further, all simulations were done in zero externally applied magnetic field and a damp-

ing of $\lambda = 0.01$ was used in all dynamical simulations. Throughout all simulations a centering procedure is employed, that keeps the DW in the middle of the length of the bar. In this way, propagation distances as long as needed can be simulated without having to worry about stray field effects should the domain wall have come close to the edges of the bar or that the DW moves out of the computational region.

Author contributions

T.Ja., J.W. and M.S. carried out the measurements and P.N., A.R. and F.T. advised on the experimental setup. P.E.R and R.M.O. developed the Landau-Lifshitz-Bloch numerical simulations code and performed the micromagnetic simulations. R.P.C. and B.L.G. grown and supplied the GaMnAsP films, Z.S. manufactured the samples and A.C.I. advised on the sample fabrication. All authors discussed the results and analysed the data. J.W., T.Ju., T.Ja. and P.E.R. wrote the paper. J.W. initiated and coordinated the project.

Competing financial interests.

The authors declare no competing financial interests

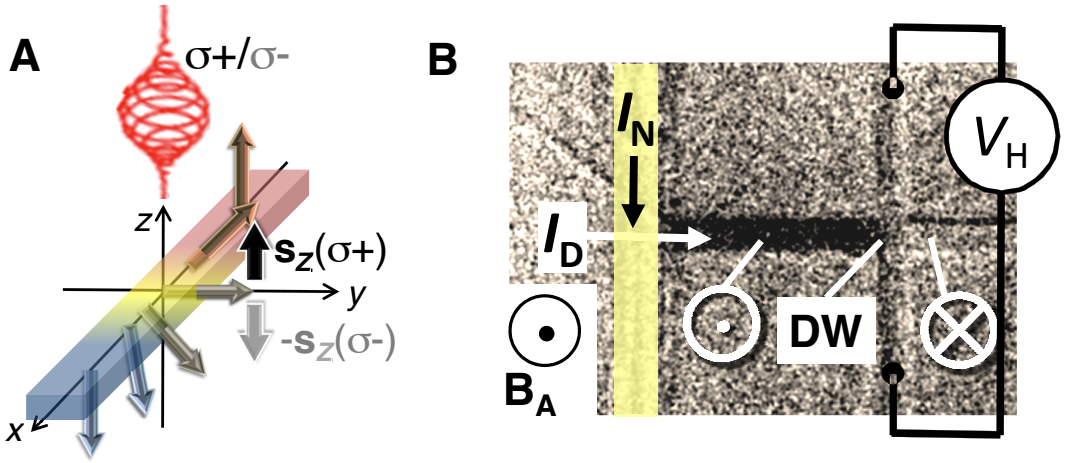

Figure 1: Optical spin transfer torque on a magnetic domain wall
(A) Sketch of light-helicity dependent optical spin transfer torque on a DW: Optically generated spin-polarised photoelectrons exert spin-transfer torque only on the rotating magnetization of the DW in the perpendicular magnetised film. Outside the DW, electron spin-polarization and magnetization are collinear.(B) Differential MOKE image of the initialized DW position where the DW is geometrically pinned at the cross entrance of a 4 μm wide Hall bar. After saturation, a reversed domain is nucleated by the Oersted field generated by the nucleation current I_{N}. Subsequently, the single DW propagates to its initial position when applying a small magnetic field of $B_{\mathrm{A}} \sim 0.2$ mT. The initial straight DW position can also be detected by a AHE measurement when applying the current I_{D} along the Hall bar. The corresponding Hall signal V_{H} corresponds to $\sim 11\%$ of the total signal upon compete magnetization reversal.

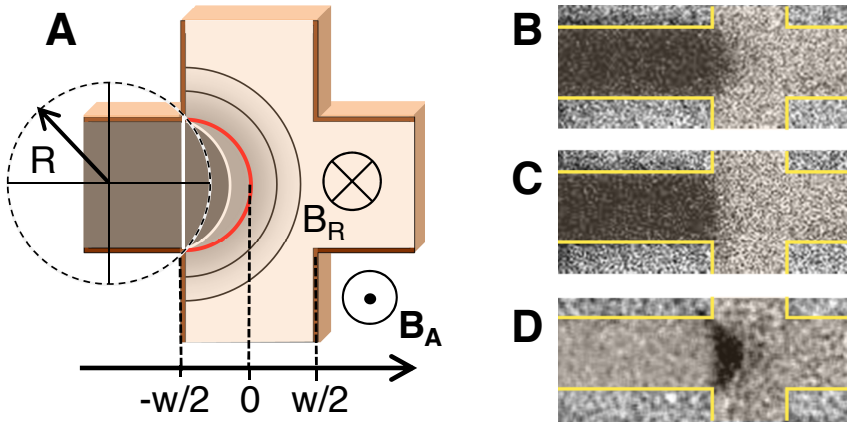

Figure 2: Soap-bubble like domain wall expansion
(A) Schematic sketch of soap-bubble like extension of an elastic DW within a symmetrical cross under the application of a magnetic field: The domain wall stays pinned on the input corners until it reaches the cross center (red half-circle). (See Supplementary Note 1.) (B) Differential MOKE images of domain configurations in case of a geometrically pinned DW in a 6μm wide device at $B_{\mathrm{A}} = 0.25$ mT (B) and after the field has been switched off ($B_{\mathrm{A}} = 0$ mT) (C). (D): Bubble like domain shape when subtracting (C) from (B). Note that the DW switched back after the field has been switched off.

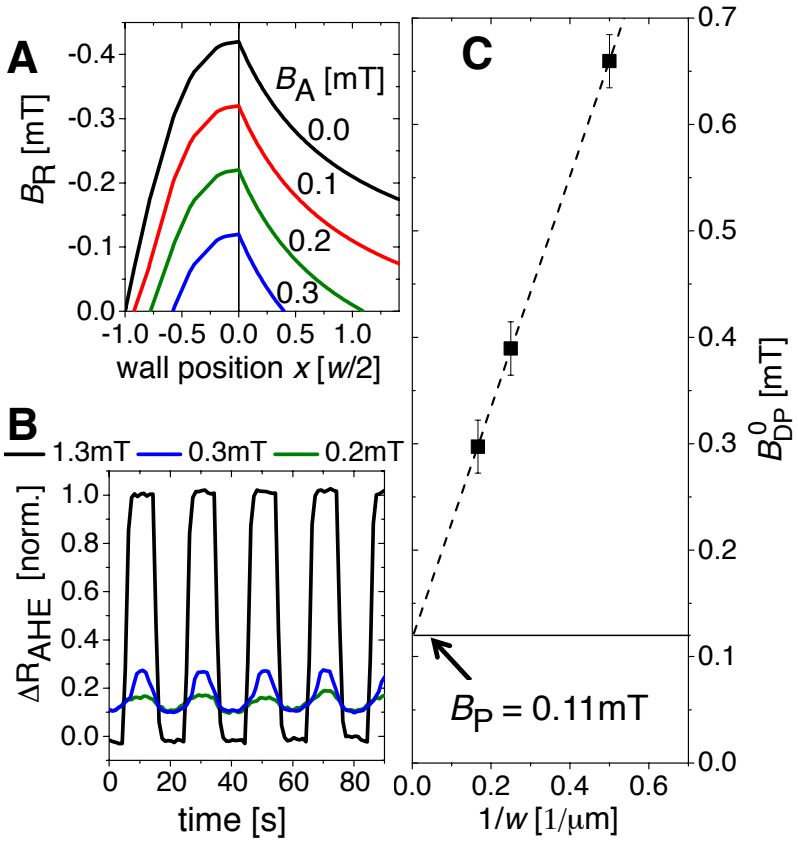

Figure 3: Repulsing motion of a geometrically pinned domain wall
(A) Effective restoring field B_{R} as a function of DW position opposing wall propagation at various applied magnetic fields B_{A} calculated for a $w = 4$ μm wide cross bar device. $|B_{\mathrm{R}}|$ becomes maximal when DW reaches the cross center. (B) Relative change of AHE signal (normalized to the total AHE signal upon compete magnetization reversal) of a 4 μm wide device due to elastic DW repulsive motion driven by an alternating field excitation $B_{\mathrm{A}} = B_0|\sin(\omega \cdot t)|$ with $B_0 = 0.2$mT, (green), $B_0 = 0.3$ mT, (blue). AHE signal for complete magnetization reversal with $B_{\mathrm{A}} = 1.3$ mT$\cdot\sin(\omega \cdot t)$, (black). (C) Experimentally determined depinning fields of 3 different devices with bar widths of $w = 2, 4$ and 6 μm. B^0_{DP} corresponds to the lowest applied magnetic field necessary to depin the DW from the cross without LP irradiation and is equal to $|B^{\mathrm{max}}_{\mathrm{R}}| + B_{\mathrm{PR}}$, B_{PR} is the DW propagation field of the unpatterned magnetic film. The broken line corresponds to the theoretical prediction from our simple propagation model (See Supplementary Note 1). The error bars of the depinning fields correspond to the standard deviation derived from 10 individual measurements.

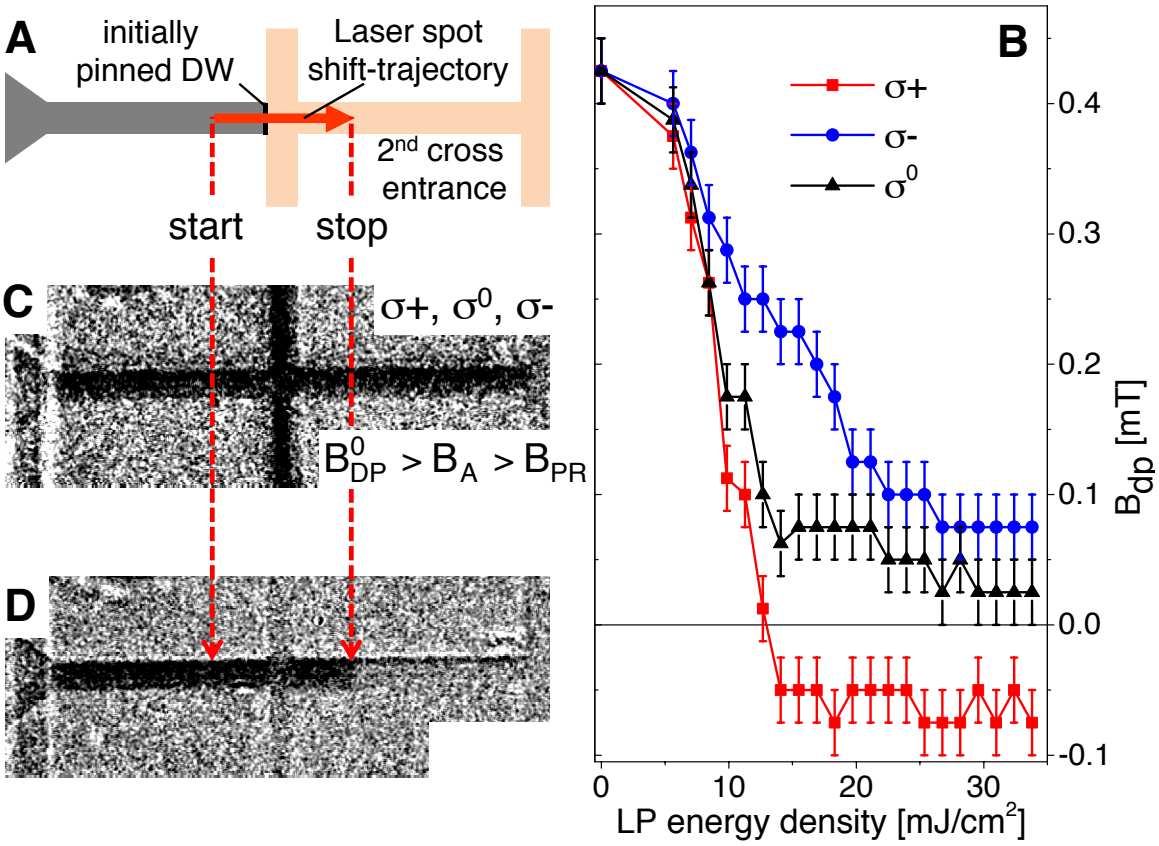

Figure 4: Helicity dependent magnetic domain wall depinning
(A) Experiment: To obtain B_{DP}, we first saturate the magnetization in a strong negative field. Then, a reversed domain is nucleated and a DW is positioned at the cross entrance. The laser pulse (LP) spot is now focused to its 'start' position 10 μm away from the initial DW location within the reversed domain. Subsequently, the spot is swept by 20 μm along the bar crossing the initial DW position with a velocity of $\sim$ 2 μm/ms. Starting from a small negative applied field of B_{A} = - 0.1 mT, DW depinning is inferred from AHE measurements and differential MOKE micrographs taken after the laser spot sweep at constant B_{A}. If the DW is still located at the cross entrance, B_{A} is increased by +0.025 mT followed by another laser spot sweep and subsequent AHE and MOKE detection. This procedure is repeated with stepwise increased B_{A} until DW depinning is detected. Each individual data-point of B_{DP} is obtained as the average from 5 independent depinning field measurements. The error bars correspond to the maximal observed scatter of B_{DP} around the corresponding mean values. (B) Depinning field B_{DP} as a function of LP energy density for circularly left (red), linearly (black) and circularly right (blue) polarized light up to the highest LP energy density where the temperature increase due to LP heating does not exceed the Curie temperature of the magnetic film. Depinning at zero applied field is only observed if the oSTT is generated by σ^+ polarised LPs. (C) Final domain configuration after laser sweeps with an applied field larger than propagation field B_{PR} and (D) at zero or small negative applied magnetic field.

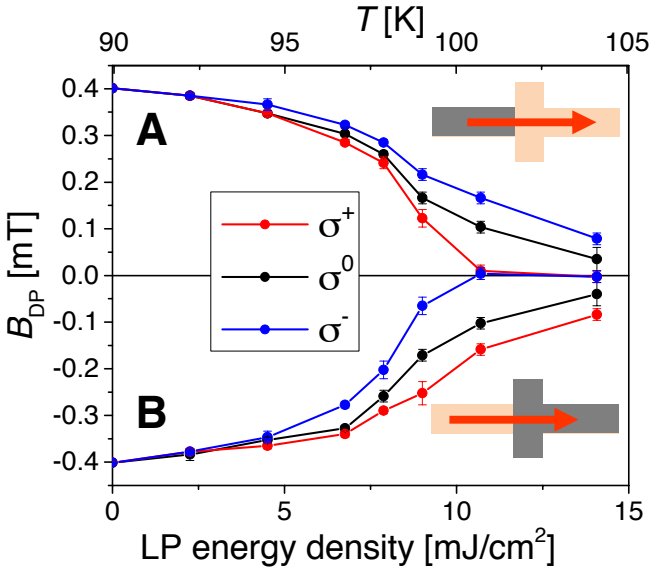

Figure 5: Helicity dependent depinning field at reversed magnetic domain configuration Depinning field B_{DP} as a function of LP energy density for circularly left (red), linearly (black) and circularly right (blue) polarized light with positive (A) and negative (B) nucleated domain magnetization. The LP related temperature increase estimated from the comparison between $B_{\mathrm{DP}}(\sigma^0, T = 90\ \mathrm{K})$ and $B_{\mathrm{DP}}(0,\ T)$ is plotted at the top of the graph.

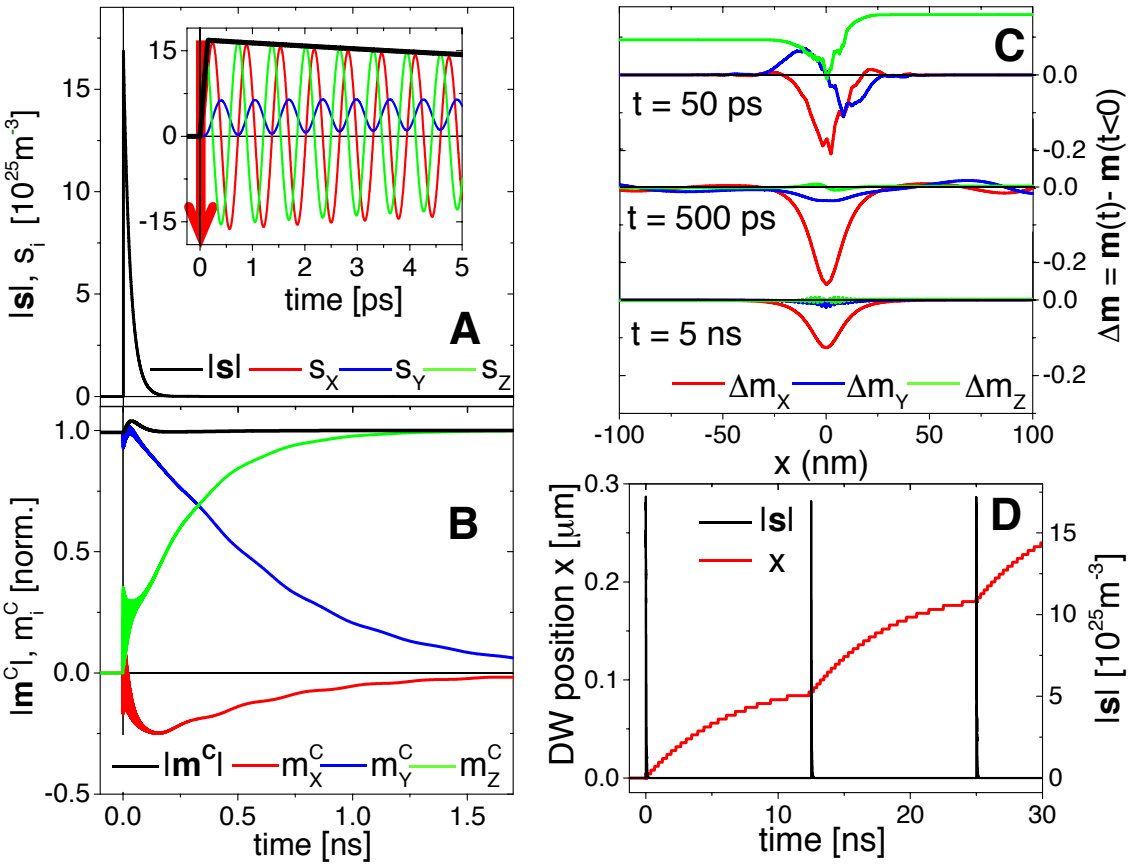

Figure 6: Dynamics of coupled photo-electron spin density and DW magnetization (A) Simulated time evolution of photo-electron spin density $\mathbf{s}$ at the center of the DW generated by a 150 fs long LP indicated as a red arrow. Inset: The x, y, z-components of $\mathbf{s}$ vs. time t showing the fast precession around the exchange field of magnetization $\mathbf{m}$. The red arrow in the inset indicates the LP. (B) The components of $\mathbf{m}$ and $|\mathbf{m}|$ vs. t at a fixed position corresponding to the initial DW center $\mathbf{m}^{\mathrm{C}}$. At $t = 0$, $\mathbf{m}^{\mathrm{C}}$ is oriented along the y-direction at the center of the Bloch-like DW. Note that $\mathbf{m}^{\mathrm{C}}$ has been normalized by its modulus before the LP is applied. The graph shows a fast initial excitation due to the LP and a damped fast jiggling during the recombination time of the photo-electrons. During this short time, angular momentum is transferred from $\mathbf{s}$ to $\mathbf{m}^{\mathrm{C}}$ causing a deformation of the DW. Note, that during the oSTT, the magnitude of $|\mathbf{m}^{\mathrm{C}}|$ increases due to the interaction between the non-zero y-component of the precessing spin density and the magnetisation at the DW center oriented initially also along y. (C) Time evolution of the DW deformation $\Delta\mathbf{m}$ along the DW width. The 3 plots show the time-evolution of the deviation from the undisturbed DW profile in the rest frame of the domain wall with zero at the DW center after the pulse was applied. The slowly relaxing DW deformation causes the DW motion. (D) The DW position as a function of time for the first three σ^+ polarized LPs (a pulse occurs every 12.5 ns). In (A)-(D), $\tau_{\mathrm{rec}} = 30$ ps and $R = 1.2 \times 10^{39}\mathrm{m}^{-3}\mathrm{s}^{-1}$.

References and Notes

1. J. Rhensius, *et al.*, Imaging of Domain Wall Inertia in Permalloy Half-Ring Nanowires by Time-Resolved Photoemission Electron Microscopy, *Phys. Rev. Lett.* **104**, 067201 (2010).

2. L. Thomas, R. Moriya, C. Rettner, S. S. P. Parkin, Dynamics of Magnetic Domain Walls Under Their Own Inertia, *Science* **330**, 1810 -1813 (2010).

3. J.-Y. Chauleau et al., Automotion versus spin-transfer torque, *Phys. Rev. B.* **82**, 214414 (2010).

4. S.-H. Yang, K.-S. Ryu, S. Parkin, Domain-wall velocities of up to 750ms^{-1} driven by exchange-coupling torque in synthetic antiferromagnets, *Nat. Nanotechnol.* **10**, 221 - 226 (2015).

5. J. Vogel, *et al.*, Direct Observation of Massless Domain Wall Dynamics in Nanostripes with Perpendicular Magnetic Anisotropy, *Phys. Rev. Lett.* **108**, 247202 (2012).

6. C. D. Stanciu, *et al.*, All-Optical Magnetic Recording with Circularly Polarized Light, *Phys. Rev. Lett.* **99**, 047601 (2007).

7. C.-H. Lambert, *et al.*, All-optical control of ferromagnetic thin films and nanostructures, *Science* **345**, 1337 - 1340 (2014).

8. A. J. Ramsay, *et al.*, Optical Spin-Transfer-Torque-Driven Domain-Wall Motion in a Ferromagnetic Semiconductor, *Phys. Rev. Lett.* **114**, 067202 (2015).

9. E. De Ranieri, *et al.*, Piezoelectric control of the mobility of a domain wall driven by adiabatic and non-adiabatic torques, *Nat. Mater.* **12**, 808 - 814 (2013).

10. P. Němec, Experimental observation of the optical spin transfer torque, *et al.*, *Nat. Phys.* **8**, 411 - 415 (2012).

11. J. Wunderlich, *et al.*, Influence of Geometry on Domain Wall Propagation in a Mesoscopic Wire, *IEEE Trans. Mag.* **37**, 2104 (2001).

12. G. E. Pikus, A. N. Titkov, in *Optical Orientation*, F. Meier, B. P. Zakharchenya, Eds. (North-Holland, Amsterdam, 1984), p. 73.

13. J.-P. Tetienne, *et al.*, Nanoscale imaging and control of domain-wall hopping with a nitrogen-vacancy center microscope, *Science* **344**, 1366 - 1369 (2014).

14. C. Schieback, D. Hinzke, M. Klaui, U. Nowak and P. Nielaba, Temperature dependence of the current-induced domain wall motion from a modified Landau-Lifshitz-Bloch equation, *Phys. Rev. B.* **80**, 214403 (2009).

15. A.V. Khvalkovskiy, K. A. Zvezdin, Ya.V. Gorbunov, V. Cros, J. Grollier, A. Fert, and A. K. Zvezdin, High Domain Wall Velocities due to Spin Currents Perpendicular to the Plane, *Phys. Rev. Lett.* **102**, 067206 (2009).

16. AC. T. Boone, J. A. Katine, M. Carey, J. R. Childress, X. Cheng, and I. N. Krivorotov, Rapid Domain Wall Motion in Permalloy Nanowires Excited by a Spin-Polarized Current Applied Perpendicular to the Nanowire, *Phys. Rev. Lett.* **104**, 097203 (2010).

17. A. Chanthbouala, R. Matsumoto, J. Grollier, V. Cros, A. Anane, A. Fert, A. V. Khvalkovskiy, K. A. Zvezdin, K. Nishimura, Y. Nagamine, H. Maehara, K. Tsunekawa, A. Fukushima and S. Yuasa, Vertical-current-induced domain-wall motion in MgO-based magnetic tunnel junctions with low current densities, *Nature Phys.* **7**, 626 - 630 (2011).

Supplementary Information: Inertial displacement of a domain wall excited by ultra-short circularly polarized laser pulses

February 24, 2017

Supplementary Note 1: Elastic bubble expansion and geometrical pinning

To describe the geometrical DW pinning exploited in our experiment we employ a simple DW propagation model where the motion of a DW of negligible width is determined by the competition between DW energy $E_\sigma = \sigma \cdot t \cdot l$ and Zeeman energy $E_\mathrm{Z} = -2M_\mathrm{S} \cdot H_\mathrm{A} \cdot t \cdot S$. $\sigma = 4\sqrt{AK_\perp}$ is the DW energy per unit area, M_S, A, and $K_\perp$ are saturation magnetisation, exchange stiffness and effective out-of-plane uniaxial anisotropy constants, respectively, l is the DW length, S is the area of the reversed domain and t is the thickness of the magnetic layer. The 'friction' of DW motion generated by DW pinning on defects in the magnetic film is described in our model by a coercive *intrinsic* propagation field H_P which is considered to be everywhere the same. We also neglect the effect of magnetic pseudo-charges generated by DW deformation, since the radius of curvature is much larger than the width of the DW in our micrometer wide Hall-crossbar structures. We therefore consider magnetic field driven DW propagation to be governed only by the competition between DW energy and Zeeman energy.

We first consider a circular-shaped domain of radius r expanding around a nucleation center

in a magnetic plate without any geometrical restrictions. Minimizing the total energy $E_{\mathrm{TOT}} = E_\sigma + E_{\mathrm{Z}}$ yields a DW with minimal length bordering a maximal area of the reversed domain. If the wall propagates by dq, the total energy changes by

$$\frac{dE_{\mathrm{TOT}}}{dq} = \sigma t \frac{dl}{dq} - 2M_{\mathrm{S}} H_{\mathrm{A}} t \frac{dS}{dq} \equiv 2M_{\mathrm{S}}(H_{\mathrm{R}} - H_{\mathrm{A}}) 2\pi r t, \tag{1}$$

where $H_{\mathrm{R}} = (2M_{\mathrm{S}})^{-1}\sigma/r$ is hereafter defined as the *virtual* restoring field. The effective net field H_{NET} oriented along the layer normal direction, which induced the DW propagation, contains in addition to the applied field H_{A}, the propagation field H_{P} and the damping torque field H_α (*1*) as well as the contribution H_{R} arising from the DW curvature (*2*).

In our geometrically constricted Hall-crossbar of width w, we can also reduce the DW motion to a one dimensional problem, that of a virtually straight DW propagating at the position q with the velocity v of the real DW center, and on which a restoring force acts due to the curvature of the real wall. Within the bar outside of the Hall cross, the DW of $l = w$ stays straight perpendicular to the stripe boundaries, and propagates in the applied magnetic field. When the DW reaches the two corners of the cross entrance, the DW must increase its length to continue propagation. The energetically optimal way is a bubble like expansion as shown in Supplementary Fig. 1 where the DW starts as a flat line (stage 'B') and remains connected to the corners of the cross entrance until it coincides with a semi-circle of radius $w/2 \equiv d$, (stage 'C'). During this process where the DW propagates from the position $q = -d \rightarrow 0$, the DW length enhances as $l = 2r \cdot \arcsin(d/r)$ and the reversed domain surface increases as $S = r^2\left[\arcsin(d/r) - (d/r)\sqrt{1-(d/r)^2}\right]$ since the DW curvature radius shrinks from $r = \infty \rightarrow d$. The relation between r and q is given by $q = r - d - \sqrt{r^2 - d^2}$. The total energy variation is given by

$$\frac{dE_{\mathrm{TOT}}}{dq} = (\sigma - 2M_{\mathrm{S}} H_{\mathrm{A}} r) t \frac{\sqrt{r^2 - d^2}\arcsin(d/r) - d}{\sqrt{r^2 - d^2} - r}. \tag{2}$$

Beyond the semi-circle (stage 'C'-'D'), the two entrance corners do no longer influence the DW propagation and the domain continues to expand circularly with increasing radius. The relation between curvature radius r and propagation coordinate q is now $r = q + d$ and the energy variation leads to

$$\frac{dE_{\mathrm{TOT}}}{dq} = (\sigma - 2M_{\mathrm{S}}H_{\mathrm{A}}r)t\pi. \tag{3}$$

The equilibrium condition $dE_{\mathrm{TOT}}/dq = 0$ leads to the applied magnetic field at which restoring and driving forces are balanced: $H_{\mathrm{R}}(q) = \frac{\sigma}{2M_{\mathrm{S}} \cdot r'}$ within the range of $q = -w/2 \rightarrow 0$, $q = r' - d - \sqrt{r'^2 - d^2}$ and $H_{\mathrm{R}}(q) = \frac{\sigma}{2M_{\mathrm{S}}[q+d]}$ within the range of $q = 0 \rightarrow (\sqrt{5} - 1)d$, hence, the maximum of the restoring field

$$H_{\mathrm{R}}^{\mathrm{max}} = \frac{\sigma}{M_{\mathrm{S}}w} \tag{4}$$

is reached, when the DW reaches the cross center at $q = 0$.

According to our model, both virtual restoring field H_{R} and the intrinsic propagation field H_{P} oppose the DW propagation. Thus, DW propagation without thermal activation will start as soon as the applied field exceeds the value of $H_{\mathrm{R}} + H_{\mathrm{P}}$. In contrast to H_{P}, the restoring field $H_{\mathrm{R}}(q)$ is a function of DW position and the model predicts a maximum restoring field at the center of the cross. Since $H_{\mathrm{R}}^{\mathrm{max}}$ is inverse proportional to the bar width, larger pinning in narrower bars is expected. Indeed, our experimental findings shown in the main text (Fig. 2) are in very good agreement with the theoretical pretictions of our model and confirm that the geometrical pinning dominates by far the intrinsic pinning and also possible pinning at the pair of exit corners (stage 'D') due to demagnetisation field inhomogeneities (*2*).

In the same spirit, virtual restoring field and intrinsic pinning on defects oppose DW motion when the driving mechanism is optical spin-transfer torque generated by circularly polarised laser pulses (LPs). This allows us to relate a measure of the oSTT driven domain wall motion to the geometrical pinning strength which is always measured as a reference quantity in a field

assisted depinning experiment without irradiation. In Supplementary Fig. 2, we present data of polarisation dependent depinning fields B_{dp} of 2, 4 and 6 μm wide crossbar devices as a function of LP energy density. Without laser irradiation, B_{dp} is largest for the narrowest bar. Thermal heating by the LP irradiation, however, is more efficient for the narrower device so that the reduction of B_{dp} is faster with increasing LP energy density for the narrower bars. We performed experiments also at a higher and lower temperature, Supplementary Fig. 2 C,D. The comparison of the 75K and 95K measurements, shown below, indeed confirms that oSTT is present independently of the sample temperature. At lower temperatures, depinning without additional applied magnetic field is realised at even lower laser powers.

Supplementary Note 2: Micromagnetic method

2.1: Landau-Lifshitz-Bloch approach (LLB)

We state again here firstly the governing equations as the forthcoming description is centered around them: The time evolution of the magnetization **m** in the LLB approach (*3*) and the spin-density **s** (*4*) read :

$$\frac{\partial \mathbf{m}}{\partial t} = -\gamma \mathbf{m} \times \mathbf{H}_{\text{eff}} + \mathbf{\Gamma}_{\text{tr}} + \mathbf{\Gamma}_{\text{lt}} \tag{5}$$

$$\frac{\partial \mathbf{s}}{\partial t} = \frac{-J_{\text{ex}}}{\hbar m_{eq}} \mathbf{s} \times \mathbf{m} + R(t)\hat{\mathbf{n}} - \frac{\mathbf{s}}{\tau_{\text{rec}}} \tag{6}$$

We start by describing Eq.(5): There, **m** is the magnetization at temperature T, normalized by the zero temperature saturation magnetization M_0 , γ is the gyromagnetic ratio and $\mathbf{H}_{\text{eff}}$ is the effective field (as described later on). M_0 was determined by extrapolation of SQUID-data and is here 35.5 kA/m. The first term on the right hand-side of Eq. (1) describes the precession of **m** around $\mathbf{H}_{\text{eff}}$ while the second term $\mathbf{\Gamma}_{\text{tr}}$=$-\frac{\gamma\alpha_\perp}{m^2}\mathbf{m} \times (\mathbf{m} \times \mathbf{H}_{\text{eff}})$ is the transverse torque with an associated damping $\alpha_\perp(T)$=$\lambda\left(1 - \frac{T}{3T_{\text{C}}}\right)$, resulting in relaxation of **m** into the direction of $\mathbf{H}_{\text{eff}}$. Here, λ is the microscopic damping parameter at T=0.

The first and second terms on the right hand-side of Eq.(5) constitute the torques included in the LLG description. In the LLB equation, a third term, $\mathbf{\Gamma}_{\text{lt}}=\frac{\gamma\alpha_{||}}{m^2}\left(\mathbf{m}\cdot\mathbf{H}_{\text{eff}}\right)\mathbf{m}$ is present, allowing for a longitudinal variation of $\mathbf{m}$; in other words $|\mathbf{m}|$ is not conserved and is allowed to fluctuate with an associated damping parameter $\alpha_{||}(T)=\frac{2T\lambda}{3T_{\text{C}}}$ beacuse, at elevated temperatures, all atomic spins whose ensemble form the corresponding $\mathbf{m}$ in a computational cell, are not necessarily all parallel to each other at all times (which is the assumption and a constraint in LLG-micromagnetics). Further, the interaction terms taken into account here result in $\mathbf{H}_{\text{eff}}=\mathbf{H}_{\text{d}}+\mathbf{H}_{\text{ex}}+\mathbf{H}_{\text{mf}}+\mathbf{H}_{\text{k}}+\mathbf{H}_{\text{OSTT}}+\mathbf{H}_{\text{r}}$, which are, demagnetizing, exchange, internal material field, uniaxial magnetocrystalline anisotropy, optical spin transfer torque and geometrical pinning -fields ($\mathbf{H}_{\text{r}}(x)$ is taken directly from Fig. 3 A in the main text), respectively. The effective field terms are evaluated from the free energy density functional f as $\frac{-1}{\mu_0 M_0}\frac{\delta f}{\delta \mathbf{m}}$. Its temperature dependence is described in terms of the thermodynamic equilibrium functions of the pertinent material parameters; normalized equilibrium magnetization m_{eq} at a given T (normalized by M_0), exchange stiffness $A(T)$, uniaxial magnetocrystalline anisotropy, $K_{\perp}(T)$, $K_{||}(T)$ and longitudinal susceptibility $\chi_{||}(T)$. Here, the temperature dependence of m_{eq} was evaluated within the mean field approximation, by a Langevin function fit to measured SQUID-data and $\chi_{||}(T)$ was calculated as shown below. The equilibrium magnetization at $T = 90$ K is here 18 kAm^{-1}. $K_{||}$ at the temperature used in the simulations was estimated from data presented in De Ranieri et al. (*5*) taken on nominally identical GaMnAsP material. The mean values of $K_{||}$=350 Jm^{-3} and $K_{\perp}$=1.51 kJm^{-3} were determined from characterization measurements on single bar-devices at a temperature of $T = 90$ K, and the exchange stiffness constant of $A(T = 90\text{ K}) = 50$ fJm^{-1} is reasonable for $Ga_{0.94}Mn_{0.06}As_{0.9}P_{0.1}$. Implementing the values above in our bubble like DW propagation model reproduces the measured depinning fields at various bar widths. By using previously measured values valid for this temperature we avoid mean-field fitting for most material parameters and thus we are more certain of their realistic values. For dynamical simu-

lations we choose the damping parameter λ=0.01. All simulations are performed considering a base temperature of $T = 90$ K (in accordance to most of the experimental measurements). The demagnetizing field is divided into near-field and the far-field contributions and is described in terms of the demagnetizing tensor, $\hat{N}$ in the standard manner; the dipole field at point $\mathbf{r}_\mathrm{i}$ from all dipoles at points $\mathbf{r}_\mathrm{j}$ is $\mathbf{H}_\mathrm{d}^\mathrm{i}(T)$=$-m_\mathrm{eq}M_0 \sum_\mathrm{j} \hat{N}(\mathbf{r}_\mathrm{i} - \mathbf{r}_\mathrm{j}, \Delta_\mathrm{x}, \Delta_\mathrm{y}, \Delta_\mathrm{z})\mathbf{m}_\mathrm{j}$, where $\Delta_\mathrm{x,y,z}$ are the dimensions of the discretization cells used along x, y and z, respectively. For the near-field, $\hat{N}$ is evaluated by the analytical formulae for interactions between tetragonal cells as derived by Newell, Williams and Dunlop (*6*). For the far-field (here, for inter-cell distances $\geq$ 40 cells), the kernel elements of $\hat{N}$ correspond to those for point dipoles. $\hat{N}$ need only to be computed once and stored in memory. The form of $\mathbf{H}_\mathrm{d}^\mathrm{i}(T)$ is that of a spatial convolution. This convolution is then evaluated by standard FFT-techniques. The exchange field $\mathbf{H}_\mathrm{ex}(T)$=$\frac{2A(T)}{\mu_0 m_\mathrm{eq}^2 M_0}\partial_\mathbf{r}^2\mathbf{m}$, where the second derivative is computed by a finite difference three-point stencil in each spatial direction. $\mathbf{H}_\mathrm{mf}$, responsible for stabilizing $|\mathbf{m}|$ is determined by the parallel susceptibility $\chi_{||}(T)$ as $\mathbf{H}_\mathrm{mf}(T)$=$\frac{1}{2\chi_{||}(T)}\left(1 - \frac{m^2}{m_\mathrm{eq}^2}\right)\mathbf{m}$ with $\chi_{||} = (\partial m_\mathrm{eq}/\partial H)_{H\to 0}$ and H being the magnitude of an applied field. In this work, the global easy axis $\hat{\mathbf{u}}||\hat{\mathbf{z}}$ and the in-plane uniaxial anisotropy axis $\hat{\mathbf{u}}||\hat{\mathbf{y}}$. Each anisotropy term contributes to $\mathbf{H}_\mathrm{k}(T)$ as $\mathbf{H}_\mathrm{k}(T)$=$\frac{2K(T)}{\mu_0 m_\mathrm{eq}^2(T) M_0}(\mathbf{m}\cdot\hat{\mathbf{u}})\hat{\mathbf{u}}$. The last effective field term, $\mathbf{H}_\mathrm{r}(T)$ is based on the considered pinning field profile for a bubble domain pinned at a cross, while the effect of temperature is taken into account by considering the reduction of $|\mathbf{B}_\mathrm{dp}|$ for σ^0-light at the laser fluency corresponding to DW depinning for σ^+-light. Therefore, the maximum $|\mathbf{H}_\mathrm{r}(T)|$ used in the simulation corresponds to 0.1 mT. As it acts as to pull the DW in the opposite direction of its excited motion, then in the simulations, the direction of the virtual restoring field $\mathbf{H}_\mathrm{r}(x)$ is along the $\mp z$-direction if the DW moves along the $\pm x$-direction. Finally, the boundary condition used for $\mathbf{m}$ on all free surfaces is $\frac{\partial \mathbf{m}}{\partial \hat{\mathbf{r}}_\mathrm{n}} = 0$, where $\hat{\mathbf{r}}_\mathrm{n}$ is the outward unit normal.

We now turn to Eq.(6) and its coupling to Eq.(5). Here, J_ex is the exchange coupling between

photo-induced electrons and the local magnetization $\mathbf{m}$. We use J_{ex}=$JS_{\text{Mn}}c_{\text{Mn}}$, where J=10 meVnm^3, S_{Mn}=5/2 is the local Mn-moment and $c_{\text{Mn}} \sim 1$ nm^{-3} is the typical moment density (***?***). When coupling to the LLB-equation we assume a temperature variation of the effective exchange coupling to the macro-vector **m** at increased T and for simplicity assume $J_{\text{ex}} \rightarrow J_{\text{ex}}m_{\text{eq}}^2$. The first term on the right hand-side of Eq.(6) describes the precession of **s** around the exchange field produced by **m** (in this step the effect of **m** on **s** is established) while the second term gives the injection of spin-polarized electrons with R being the rate per unit volume and $\hat{n}$ the initial spin polarization direction defined by the helicity of the light with $\hat{\mathbf{n}}$=[00$\pm$1]. Finally, the third term represents the decay of the photo-carrier spin with a life-time of τ_{rec}, limited in our case by the carrier-recombination time. Based on previous measurements in literature, we set τ_{rec}=30 ps. Gradient terms in **s** are neglected. During precession, **s** transfer its angular momentum to **m**. The precession time of **s** is very fast as compared to the natural precession of **m** (~ 100 fs versus ~ 1 ns). The absorption of angular momentum from **s** results in a torque on **m**. This torque is then entered into Eq.(5) by an augmentation to the rest of the effective field by $\mathbf{H}_{\text{OSTT}}$ (thus the effect of **s** on **m** is established); The interaction energy density between **s** and **m** is f_{ex}=$\frac{-J_{\text{eff}}(T)}{m_{\text{eq}}}\mathbf{s} \cdot \mathbf{m}$. The corresponding effective field term is then according to the definition in the preceeding paragraph, $\mathbf{H}_{\text{OSTT}}(T)$=$\frac{J_{\text{eff}}(T)}{\mu_0 m_{\text{eq}} M_0}\mathbf{s}$. Equations (1) and (2) are solved together using a 5^{th} order Runge-Kutta integration scheme.

2.2: Computational geometry and simulation procedure

We consider a one-dimensional bar with 4095 x 1 x 1 computational cells composing a structure as shown in Supplementary Fig. 3. The cell dimension is 4 nm x 4 μm x 25 nm. A Bloch DW is initialized in the center of the bar and let to relax quickly with strong damping by setting λ=0.9. This configuration is then used as a starting configuration for the simulations of domain wall motion under the light pulses.

Once the domain wall is prepared, circularly polarized light is pulsed at a rate of 80 MHz. The length of each pulse is set to 150 fs. For the simulation of the depinning process, the spin-polarized carrier injection rate is $R = 1.225 \times 10^{39}\mathrm{m}^{-3}\mathrm{s}^{-1}$. This order of magnitude for R is required for the DW to escape the elastic pinning potential. The equivalent pulse power corresponds to the time-averaged laser power used in the experiments of the order of 20 mW assuming a skin depth of 1 μm. Further, all simulations were done in zero externally applied magnetic field and a damping of $\lambda = 0.01$ was used in all dynamical simulations.

Throughout all simulations a centering procedure is employed, that keeps the DW in the middle of the length of the bar. In this way, propagation distances as long as needed can be simulated without having to worry about stray field effects should the domain wall have come close to the edges of the bar or that the DW moves out of the computational region.

Supplementary Fig. 4 shows the calculated time-averaged DW velocity v_{DW} as a function of LP energy density. We identify the Walker breakdown peak velocity of about 5 m/s at about 18 mJ/cm^2 for the DW with only out-of-plane magnetic anisotropy. Stabilising the DW structure, e.g., by DMI or by introducing additional anisotropy via mechanical strain, can shift the WB to higher values and allow for achieving higher DW velocities, (*5*). We show in Supplementary Fig. 4 that indeed higher velocities can be achieved when the static structure of the DW is stabilised by introducing additional uniaxial in-plane anisotropy. We finally note that the limiting speed for any texture to propagate in a given magnetic material is the magnon group velocity $\mathrm{v_m}$. We estimate $v_{\mathrm{m}} = 4 \cdot J \cdot S_{\mathrm{Mn}} \cdot a/\hbar$ using the parameter of our GaMnAsP film at $T = 90$ K, a is the spin separation length and J is the next neighbour exchange constant. With $\mathrm{J_{ex}} = A \cdot a/(2S_{\mathrm{Mn}}^2)$ and $a = (2 \cdot g \cdot \mu_{\mathrm{B}} \cdot S_{\mathrm{Mn}}/M_S)^{1/3}$ (g is the Lande factor and μ_{B} is the Bohr magneton) we obtain $v_{\mathrm{m}} \approx 1$ km/s.

Supplementary Note 3:
Additional experimental evidences for optical spin transfer torque driven DW motion

3.1: Wavelength dependency of helicity dependent DW motion

We have performed wavelength dependent experiments to support the optical spin transfer torque origin of the helicity dependent LP induced DW motion. In experiments described in the main text we use LP excitation with a wavelength λ = 750 nm that excites photo-electrons slightly above the bottom of the GaAs conduction band so that for a circularly polarized incident light, photo-electrons become spin-polarized with the degree of polarization approaching the maximum theoretical value of 50% (*7*). At energies above and below band gap energy (Supplementary Fig. 5), the spin polarisation of the photo-electrons is reduced. Photons excitation at higher energies results in the reduction of net-photoelectron spin-polarisation mainly because carrier excitation from the split-off valence band can take place. The photocarrier generation from low-energy photons with sub-band gap energies comes mainly from excitation of impurity states within the band gap.

3.2: Dependency of helicity dependent DW motion on the sweep direction of the focused laser spot

We now investigate the effect of the thermal gradients generated by the laser spot on the helicity dependent DW depinning. By inverting the sweep direction of the focused LP spot with respect to the geometrically pinned DW, we invert also the thermal gradient affecting the DW. In case that the LP spot approaches from the reversed domain along the patterned bar, Supplementary Fig. 6A, both $B_{\mathrm{dp}}(\sigma^+)$ and $B_{\mathrm{dp}}(\sigma^-)$ decrease faster compared to the situation where the laser spot approaches from the unreversed domain (Supplementary Fig. 6B). This observation is explained by the stronger temperature increase from LP heating in the narrow bar compared to

the lower temperature rise in the wider cross area. On the other hand, the helicity dependence of B_{dp}, which is of oSTT origin, remains unaffected by the LP sweep direction.

3.3: Continuous wave excitation vs. laser pulse excitation

We now show that the DW can be also moved by a focused laser spot of continuous wave (cw) excitation. To compare the efficiency of the cw-excitation with our ultrashort LP-excitation approach we have deduced $B_{\text{dp}}(\sigma^+)$ and $B_{\text{dp}}(\sigma^-)$ for LP- and cw-excitation at the same averaged laser power P_{av}. Based on our LLB approach, we also have calculated DW propagation driven by oSTT from LP- and cw- excitations. From the simulations, we have derived the averaged DW velocity vs. P_{av} at the position of maximal restoring field (Supplementary Fig. 7A). Positive averaged velocities correspond therefore to the depinning of the DW. For zero or negative velocities, the DW remains pinned. Both calculation and experimental results presented in Supplementary Fig. 7 confirm that a DW can be depinned via oSTT generated by ultrashort LP and by cw-excitation. However, cw-driven DW propagation requires always higher averaged laser power (Supplementary Fig. 7A). Comparing $B_{\text{dp}}(\sigma^-, \sigma^+)$ (Supplementary Fig. 7B, C) for the two excitation schemes at equal averaged laser power shows a stronger efficiency of the pulsed oSTT. Moreover, the effect of laser heating on DW depinning is stronger in case of cw-excitation compared to ultrashort LP-excitation. Therefore, helicity dependent inertial DW motion induced by ultrashort LP is more efficient than DW motion induced by constant excitation.

3.4: Temperature dependent depinning field

The temperature dependence of the resistance of the magnetic bar is used to monitor and control the actual sample temperature (Supplementary Fig. 8A). In order to obtain the accurate resistivity dependence of our devices we performed a reference measurement in a bath cryostat, where

the (Ga,Mn)(As,P) sample is thermally anchored to a calibrated temperature sensor and where the temperature dependent resistivity $R(T)$ of (Ga,Mn)(As,P) is monitored during heating-up from 4 K to room temperature. The Curie temperature $Tc = 115$ K is obtained by identifying the cusp in dR/dT (*8*), (Supplementary Fig. 8A). We have determined B_{dp} without laser irradiation at a 4 μm wide device as a function of temperature in a temperature range below $T = 90$ K until close to Curie-temperture (Supplementary Fig. 8B). This allows us to estimate an effective sample temperature deduced from the comparison between temperature dependent measurements of B_{dp} without irradiation and measurements of $B_{\text{dp}}(\sigma^0)$ vs. P_{av} laser power and at fixed base temperature (*9*).

3.5: MCD induced temperature gradients

In this section, we identify the sign and estimate the magnitude of the temperature gradient generated by MCD between two opposite magnetized domains. We use a 6 μm wide, 18 μm long (contact-to-contact) bar-device patterned from our GaMnAsP/GaAs film. LPs are focused at the center of our bar as shown in Supplementary Fig. 9. We evaluate the temperature variation at opposite saturation magnetisations from the resistance variation detected in our sample at fixed LP polarisation. We employ a sensitive double Lock-in technique and compare magnetisation dependent resistance variation with the temperature dependence of the GaMnAsP film resistivity.

To estimate the temperature variation at the irradiated spot position from the resistance variation measured in 4-point geometry over the whole bar device, we employ a simple resistor network model described in Supplementary Fig. 10. The 18 μm long and 6 μm wide bar is divided into 27 (2 μm $\times$ 2 μm) squares. Only the central square is irradiated having the resistance R^L_{sq} . All other squares remain in darkness having the equal resistances, R^D_{sq}. Within this simple resistor network model, we can estimate the temperature variations

generated by the MCD at the irradiated square of the device by detecting the total device resistance variation at opposite saturation magnetisations when comparing the measured data to a reference measurement of the temperature dependency of $\Delta = R(T)/R(90\text{ K})$, Supplementary Fig. 10, right. Since only the irradiated spot can be compared with this reference measurement, we need to relate the sample temperature variation of the spot to the measurable resistance variation of the total device as shown in Supplementary Fig. 10 (left). In the frame of this approximation, the ratio of irradiated and non-irradiated square resistances is estimated to $\Delta = R^L_{sq}/R^D_{sq} = 27R^L_T/R^D_T - 26$; ($R^L_T$, and R^D_T are the measurable total bar device resistances with and without spot irradiation). To avoid any small alternations of our focused LP spot in intensity, spot position, etc., we measure the resistance variation due to the MCD by changing periodically the sample saturation magnetisation (at a frequency of 0.2 Hz) and keeping simultaneously the LP polarisation fixed. A first Lock-in amplifier measures the 4-point resistance as the response to an alternating probe current (f = 123 Hz). After the subtraction of an offset, the output of the first Lock-in is amplified by a factor x100. The resulting signal feeds into a second Lock-in, which amplifies the signal with reference to the alternating saturation magnetisation. As a result, we obtain $\Delta R_m = R^L_{T,+M_z} - R^L_{T,-M_z}$. We evaluate $dT = T(R^L_{sq,+M_z}) - T(R^L_{sq,-M_z}) = \alpha(\Delta_{+M_z} - \Delta_{-M_z})$, with $T = \alpha\Delta$ and α is obtained from the linear slope of the temperature dependence of the sample resistance around $T = 90$ K. Since $\Delta_{+M_z} - \Delta_{-M_z} = 27(R^L_{T,+M_z} - R^L_{T,-M_z})/R^D_T = 27\Delta R_m/R^D_T$, we can estimate $dT = 27\alpha\Delta R_m/R^D_T$ with $R^D_T = 1.244\,\text{k}\Omega$.

In Supplementary Fig. 11(a,b) we show the LP polarisation dependent temperature variation at the irradiated spot between positive and negative saturation magnetisations. At $T = 90\ K$ substrate temperature, the temperature variation is of the order of $+(-)200\ mK$ for circularly polarised $\sigma^+(\sigma^-)$ LPs. Hence, the $\sigma^+(\sigma^-)$ LPs irradiated film with positive (negative) magnetisation becomes hotter than the film with negative (positive) magnetisation orientation.

In our oSTT experiments shown in Fig. 3 of the main text, we saturate the magnetic bar in a strong negative magnetic field and nucleate a reversed domain at the left side of the bar with positive magnetisation orientation . When irradiated with $\sigma^+(\sigma^-)$ polarised LPs, MCD heats up the nucleated magnetic domain more (less) than the rest of the magnetic film with negative magnetization orientation. In the experiment, we observe DW depinning and motion towards the area with negative magnetisation only when the DW is irradiated with σ^+ polarised LPs. If we repeat the experiment with inverted magnetisation (positive saturation, nucleated domain with negative magnetisation orientation) the DW moves towards the positive magnetisation orientation only when irradiated with σ^- polarised LPs. Hence, we always observe that the circularly polarised LP exposed DW moves towards the colder region, which excludes the MCD origin of the observed DW motion. Considering a DW width of ~ 50 nm (Supplementary Fig. 11C), we estimate a MCD generated heat gradient of $\sim 6 \times 10^6$ K/m. This value is smaller than the heat-gradient generated by the focused light spot independent of polarisation.

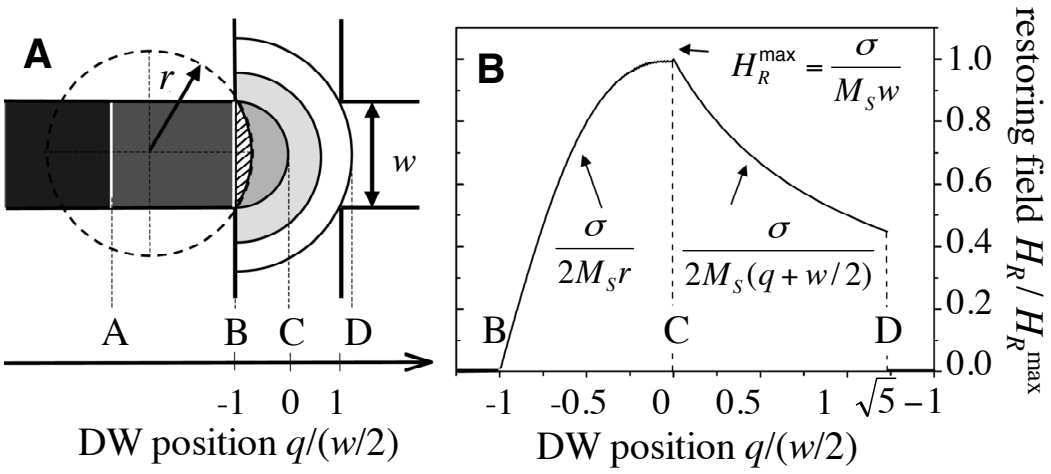

Supplementary Fig. 1: Geometrical domain wall pinning.

(A) "Soap-bubble" like expansion of a DW within a symmetric cross. The DW stays pinned on the cross input corners until stage 'C' is reached. At this position, the geometrical restoring field H_{R} reaches its maximum. (B) Position dependent *virtual* restoring field $H_{\mathrm{R}}(q)$ arising from the wall curvature is reflecting the elasticity of the wall. Introducing $H_{\mathrm{R}}(q)$ reduces our system to a one-dimensional problem, that of a virtual straight DW propagating with position q and velocity v of the real DW center.

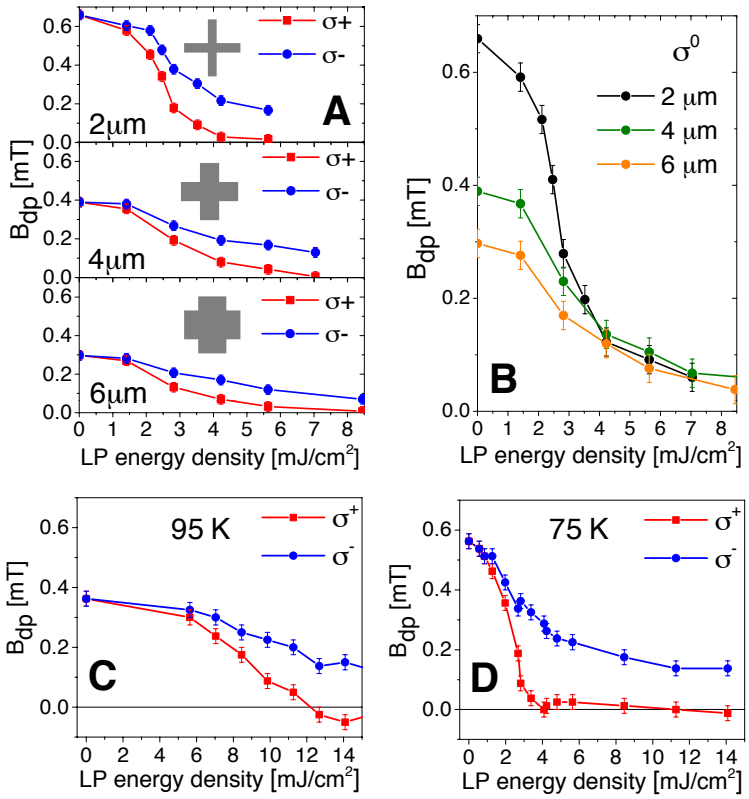

Supplementary Fig. 2: LP dependent depinning field.

Polarization dependent depinning field $B_{\rm dp}(\sigma^+, \sigma^-, \sigma^0)$ as a function of LP energy density of 2, 4 and 6 μm wide crossbars for (A) circularly ($\sigma^{+,-}$) and (B) linearly (σ^0) polarized LPs. The difference between $B_{\rm dp}(\sigma^+)$ and $B_{\rm dp}(\sigma^-)$ is due to the optical spin transfer torque and the decrease of $B_{\rm dp}$ with increaseing LP energy density is due to the heating from photon absorption. Circularly polarization dependent depinning field $B_{\rm dp}(\sigma^+, \sigma^-)$ measured at the 4 μm wide crossbars device at different sample temperatures, $T = 95K$ (C) and at $T = 75K$ (D) The error bars correspond to the maximal observed scatter of $B_{\rm dp}$ around the corresponding mean values.

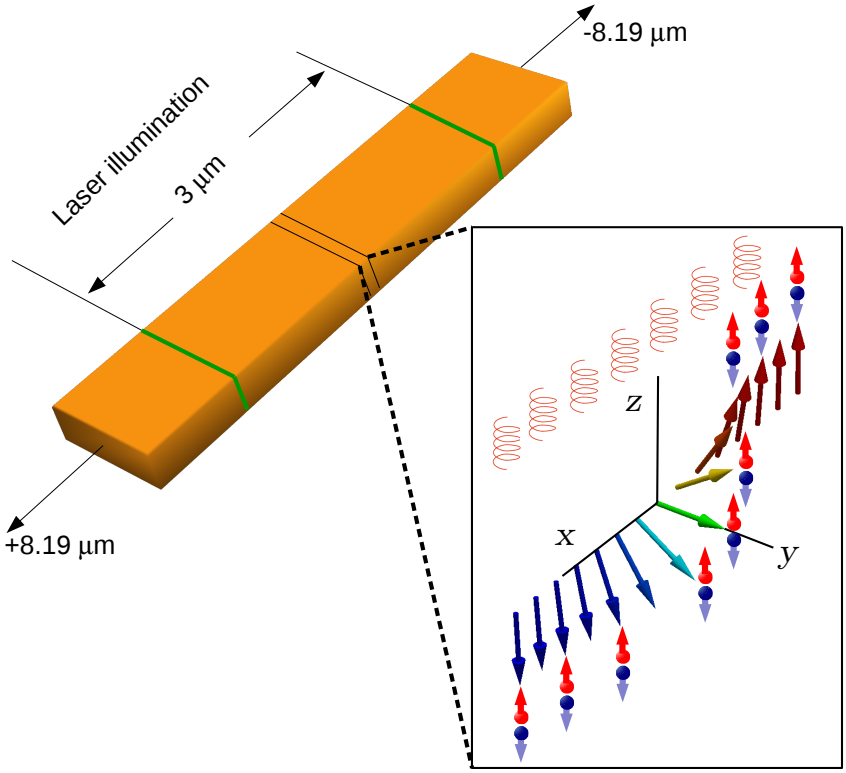

Supplementary Fig. 3: Computational Setup.

The total bar extension is 4x4095=16384 nm along x, 4 μm wide and 25 nm thick. The DW is of Bloch type, initially located at the center of the bar. Circularly polarized light is applied at constant fluency within a 3 μm long window around the domain wall. The blow-up shows the computed structure of the DW and schematically shows the spin up or spin down spin-polarized charge carriers generated by the circularly polarized light.

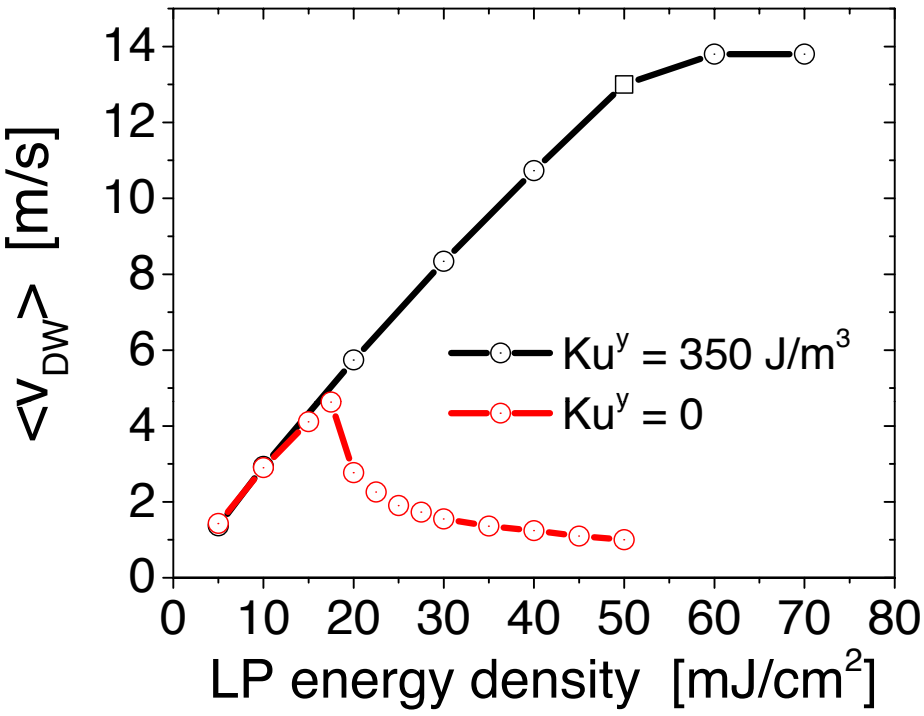

Supplementary Fig. 4: Domain Wall mobility.

DW velocity as a function of LP energy density calculated in the LLB approach. DW velocity, time averaged during the 12.5ns dark phase after a oSTT pulse, as a function of laser power for GaMnAsP film without (red) and with uniaxial inplane anisotropy Kuy (black). The uniaxial inplane anisotropy can be introduced by mechanical strain, (*5*).

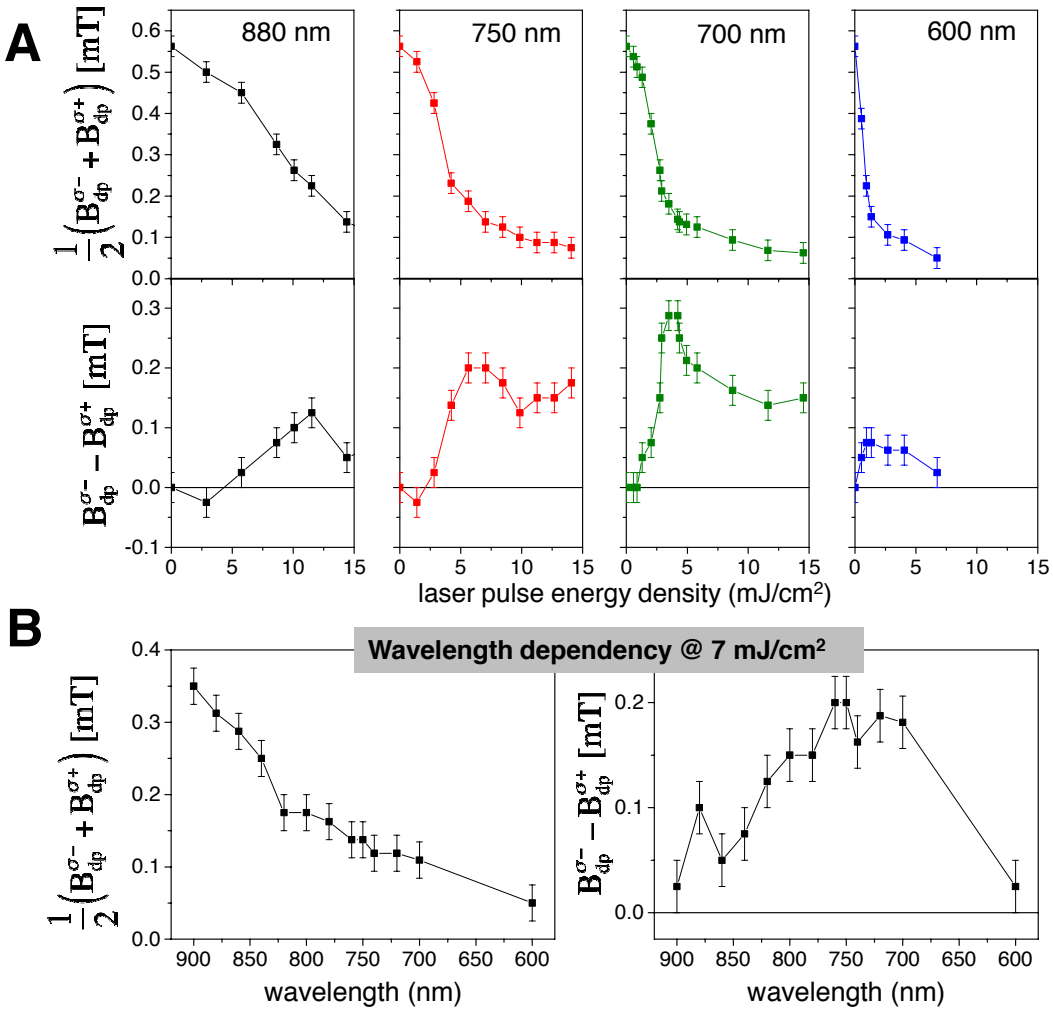

Supplementary Fig. 5: Wavelength dependent domain wall depinning.

(A) Average and difference of the depinning field B_{dp} for σ^- and σ^+ vs. LP energy density at various wavelengths at 75 K sample temperature. The average $1/2[B_{\mathrm{dp}}(\sigma^-)+B_{\mathrm{dp}}(\sigma^+)]$ indicates the reduction of the geometrical pinning due to helicity independent LP heating. The difference $B_{\mathrm{dp}}(\sigma^-) - B_{\mathrm{dp}}(\sigma^+)$ shows the effect of the oSTT on the DW motion. (B) The average at a fixed LP energy density of 7 mJ/cm^2 identifies the reduction of geometrical DW pinning with increasing LP heating due to enhanced absorption at higher photon energy. On the other hand, the difference $B_{\mathrm{dp}}(\sigma^-) - B_{\mathrm{dp}}(\sigma^+)$ shows that the oSTT efficiency is highest when the photon energy is close to the band gap of GaAs and it is strongly suppressed when photo-electrons are generated from the spin-split-off band at high energy with $\lambda = 600$ nm. The error bars correspond to the maximal observed scatter of B_{dp} around the corresponding mean values.

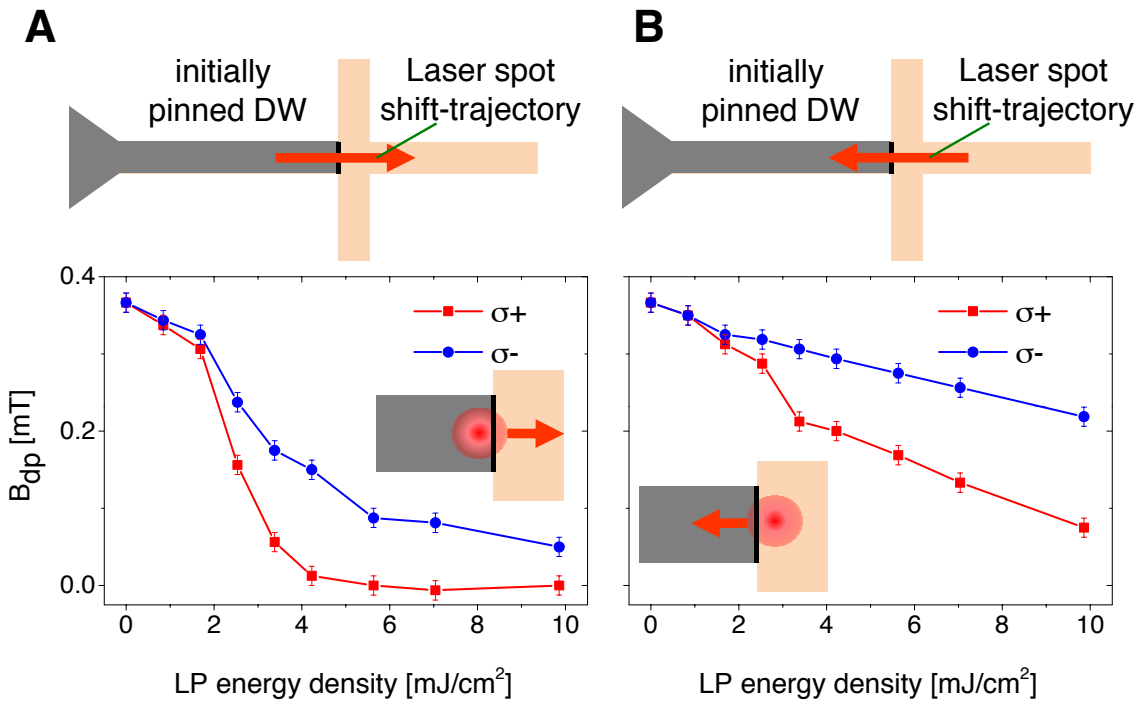

Supplementary Fig. 6: Sweep direction dependent domain wall depinning.

Depinning fields $B_{\mathrm{dp}}(\sigma^+)$ and $B_{\mathrm{dp}}(\sigma^-)$ versus LP energy density, (A), in case that the focused LP spot approaches from the narrow bar, and (B), when the LP spot approaches from the wider cross area. The error bars correspond to the maximal observed scatter of B_{dp} around the corresponding mean values.

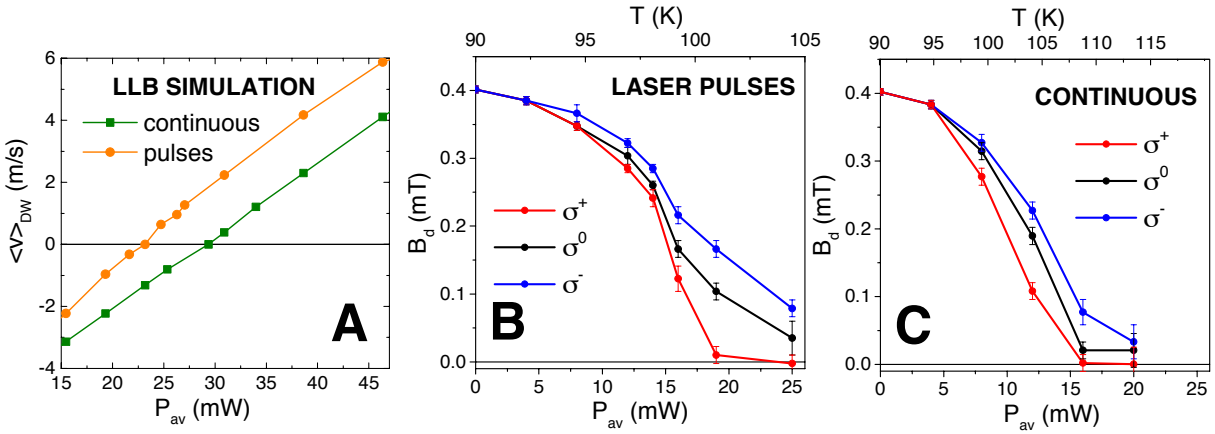

Supplementary Fig. 7: Ultrashort pulse excitation vs. continuous cw laser excitation

(A) Averaged DW velocities vs. P_{av} at the position of maximal restoring field for DW propagation driven by oSTT with ultrashort LP excitation (orange) and cw-excition (green). The averaged velocity is deduced from simulations of DW propagation based on the LLB approach. Depinning field B_{dp} vs. P_{av} for circularly (σ^+), (σ^-) and linearly polarized (σ^0) laser light in case of LP- (B) and cw-(C) excitation. We have assigned an effective sample temperature deduced from the comparison between temperature dependent measurements of B_{dp} without laser irradiation and measurements of $B_{\mathrm{dp}}(\sigma^0)$ vs. P_{av} laser power and at fixed base temperature. The error bars correspond to the maximal observed scatter of B_{dp} around the corresponding mean values.

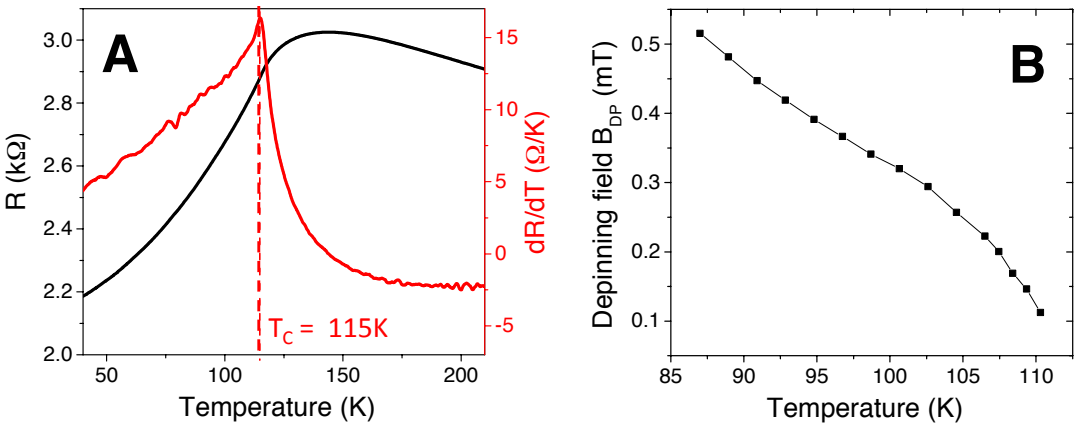

Supplementary Fig. 8: Magnetic properties of the GaMnAsP film.

(A) Temperature dependence of the resistance of a GaMnAsP bar and dR/dT identifying a Curie temperature of $Tc = 115$ K. (B) Depinning field B_{dp} without laser irradiation as a function of temperature.

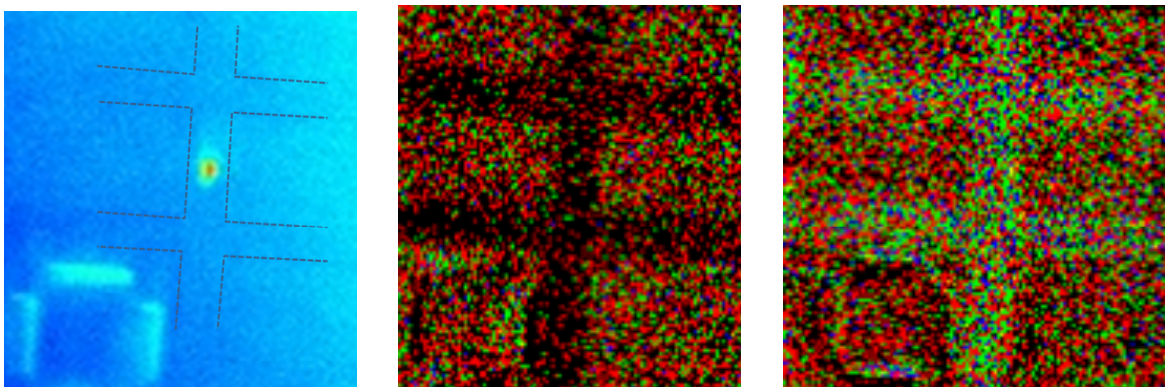

Supplementary Fig. 9: Experimental setup for MCD measurements.

Cross bar device for 4-point measurements: Left: Laser spot focused to the center of the bar between the two cross-contacts; Middle, (Right): MOKE micrographs at positive, (negative) magnetisation orientations.

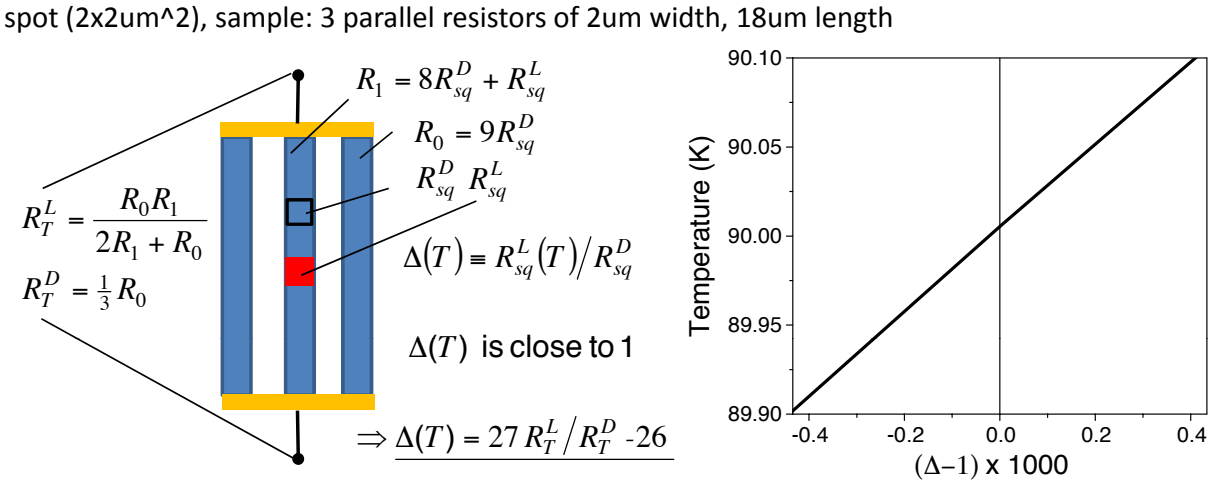

Supplementary Fig. 10: Model for MCD generated temperature variations.

Left: Simple resistor network model; Right: Resistance variations as a function of the sample temperature.

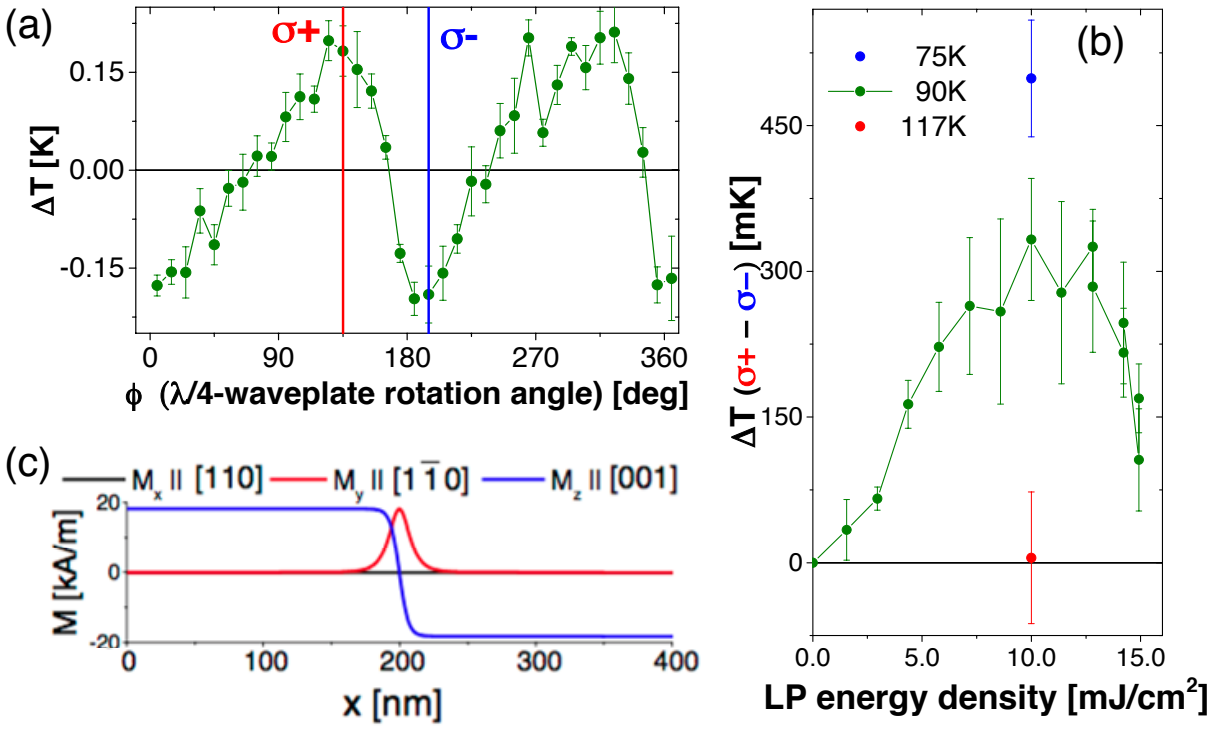

Supplementary Fig. 10: MCD induced temperature variations.

(a): Temperature variation measured at $T = 90$ K substrate temperature and for a laser power of 10 mJ/cm^2 as a function of LP polarisation. The polarisation is varied by a λ/4-waveplate. A constant offset is subtracted from all data points. Before taking a data point, we always realigned the focused laser spot to the bar center. The discrepancy between the measured angular dependence of the temperature variation from the expected $\cos(2\phi)$ behaviour is due to unintentional polarisation effects in some of the optical components in our setup. σ^+ and σ^- polarised LPs correspond to ϕ = 135 deg and ϕ = 195 deg, respectively. As expected for MCD related heating, we find largest temperature variations for σ^+ (red line) and for σ^- (blue line) polarisations. (b) MCD induced differences in temperature variation between σ^+ and σ^- as a function of LP energy density for 3 different substrate temperatures, 75 K (blue), 90 K (green), and 117 K (red). Note that the MCD induced heating disappears above the Curie temperature T_C =115 K. The error bars correspond to the standard deviation of the detected resistance variation. (c) Static DW profiles obtained by micromagnetic simulation with 0.5 nm (2 nm) discretisation length along (perp. to) a 4 μm wide bar. The simulation is based on the experimentally obtained values at T =90 K for out-of-plane uniaxial anisotropy $K_\perp$ =1500 Jm^{-3}, saturation magnetization M_S =18.2 kA/m and we use A =50 fJ/m for the exchange stiffness parameter.

Supplementary References

1. A. P. Malozemoff, J. C. Slonczewski: *Magnetic Domain Walls in Bubble Materials*, Academic Press, New York (1979).

2. J. Wunderlich: *Extraordinary Hall Effect in Multi-layered Magnetic Films: Application to the Study of Magnetization Reversal Dynamics*, ISBN-13: 978-3826591105, Shaker Verlag, Germany (2001).

3. C. Schieback, *et al.*, Temperature dependence of the current-induced domain wall motion from a modified Landau-Lifshitz-Bloch equation, *Phys. Rev. B.* **80**, 214403 (2009).

4. P. Němec, *et al.*, Experimental observation of the optical spin transfer torque, *Nat. Phys.* **8**, 411 - 415 (2012).

5. E. De Ranieri, *et al.*, Piezoelectric control of the mobility of a domain wall driven by adiabatic and non-adiabatic torques, *Nat. Mater.* **12**, 808 - 814 (2013).

6. A. J. Newell, W. Williams, D. J., Dunlop, A generalization of the demagnetizing tensor for nonuniform magnetization, J. Geophys. Res., **98** 9551-9555 (1993).

7. G. E. Pikus, A. N. Titkov, in *Optical Orientation*, F. Meier, B. P. Zakharchenya, Eds. (North-Holland, Amsterdam, 1984), p. 73.

8. V. Novák, *et al.*, Curie Point Singularity in the Temperature Derivative of Resistivity in (Ga,Mn)As, Phys. Rev. Lett. **101**, 077201 (2008).

9. S. Shihab, *et al.*, Steady-state thermal gradient induced by pulsed laser excitation in a ferromagnetic layer, J. Appl. Phys. **119**, 153904 (2016).